THESIS FOR THE DEGREE OF LICENTIATE OF ENGINEERING

Simulation and analysis of radiation from runaway electrons

MATHIAS HOPPE

Simulation and analysis of radiation from runaway electrons
MATHIAS HOPPE

Cover:
A synthetic synchrotron radiation image from a population of runaway electrons in a tokamak with circular magnetic flux surfaces.

Simulation and analysis of radiation from runaway electrons
MATHIAS HOPPE
Department of Physics
Chalmers University of Technology

Abstract

Electron runaway constitutes one of the primary threats to future toka-mak fusion reactors such as ITER. Successful prevention and mitigation of runaways relies on the development of theoretical models which ac-curately describe the dynamics of runaway electrons, and these models must in turn be validated in experiments. Experimental validation of models is however often made difficult by the fact that the diagnostic signals obtained in experiments only depend indirectly on the parti-cle dynamics. In this thesis, a synthetic diagnostic model is presented which has been implemented in the *Synchrotron-detecting Orbit Follow-ing Toolkit* (SOFT), and which bridges this divide between theory and experiment. The synthetic diagnostic calculates the bremsstrahlung and synchrotron radiation diagnostic signals corresponding to a given run-away electron population, which can be directly compared to camera images and radiation spectra obtained in experiments. Bremsstrahlung and synchrotron radiation from runaway electrons are particularly sen-sitive to the runaway dynamics and, as is shown in this thesis, they provide insight into the runaway electron distribution function.

This thesis focuses on geometric effects observed in the detected ra-diation when magnetic field inhomogeneities and detector properties are taken into account, something which previous studies have neglected. The dependence of the observed radiation on magnetic field geometry, detector properties and runaway parameters is characterised, and it is explained how geometric effects limit the otherwise monotonic growth of the diagnostic response function with the runaway pitch angle. The synthetic diagnostic model is applied to experiments in the Alcator C-Mod and the DIII-D tokamaks and is used to validate kinetic theory predictions of the electron distribution function. It is found that the kinetic model agrees well in certain scenarios and fails in others. In the scenarios where it fails, the synthetic diagnostic model suggests that a mechanism causing a larger spread in pitch angle may be missing from the kinetic model.

Keywords: plasma physics, fusion, tokamak, runaway electrons, brems-strahlung, synchrotron radiation, synthetic diagnostics

iv

Publications

A M. Hoppe, O. Embréus, R. A. Tinguely, R. S. Granetz, A. Stahl, and T. Fülöp,
SOFT: a synthetic synchrotron diagnostic for runaway electrons,
Nuclear Fusion **58**, 026032 (2018).
`https://doi.org/10.1088/1741-4326/aa9abb`

B R. A. Tinguely, R. S. Granetz, M. Hoppe, and O. Embréus,
Measurements of runaway electron synchrotron spectra at high magnetic fields in Alcator C-Mod,
Nuclear Fusion **58**, 076019 (2018).
`https://doi.org/10.1088/1741-4326/aac444`

C M. Hoppe, O. Embréus, C. Paz-Soldan, R. A. Moyer, and T. Fülöp,
Interpretation of runaway electron synchrotron and bremsstrahlung images,
Nuclear Fusion **58**, 082001 (2018).
`https://doi.org/10.1088/1741-4326/aaae15`

D R. A. Tinguely, R. S. Granetz, M. Hoppe, and O. Embréus,
Spatiotemporal evolution of runaway electrons from synchrotron images in Alcator C-Mod,
Plasma Physics and Controlled Fusion **60**, 124001 (2018).
`https://doi.org/10.1088/1741-4326/aac444`

Related publications, not included in the thesis

E   O. Embréus, L. Hesslow, M. Hoppe, G. Papp, K. Richards, and
T. Fülöp,
Dynamics of positrons during relativistic electron runaway,
Journal of Plasma Physics **84**, 905840506 (2018).
`https://doi.org/10.1017/S0022377818001010`

F   L. Hesslow, O. Embréus, M. Hoppe, T. C. DuBois, G. Papp, and
T. Fülöp,
*Generalized collision operator for fast electrons interacting with
partially ionized impurities*,
Journal of Plasma Physics **84**, 905840605 (2018).
`https://doi.org/10.1017/S0022377818001113`

G   M. Hoppe, O. Embréus, A. Tinguely, R. Granetz, A. Stahl, and
T. Fülöp,
Synthetic synchrotron diagnostics for runaway electrons,
Proceedings of the 44th EPS Conference on Plasma Physics,
Belfast, P5.151 (2018).
`http://ocs.ciemat.es/EPS2017PAP/pdf/P5.151.pdf`

H   M. Hoppe, O. Embréus, P. Svensson, L. Unnerfelt, and T. Fülöp,
*Simulations of bremsstrahlung and synchrotron radiation from
runaway electrons*,
Proceedings of the 45th EPS Conference on Plasma Physics,
Prague, O5.J603 (2018).
`http://ocs.ciemat.es/EPS2018PAP/pdf/O5.J603.pdf`

I   O. Embréus, K. Richards, G. Papp, L. Hesslow, M. Hoppe, and
T. Fülöp,
Dynamics of positrons during relativistic electron runaway,
Proceedings of the 45th EPS Conference on Plasma Physics,
Prague, P5.4011 (2018).
`http://ocs.ciemat.es/EPS2018PAP/pdf/P5.4011.pdf`

Contents

Acknowledgments

I have now been involved with the Plasma Theory group at the Department of Physics for close to four years, one and a half of which as a PhD student, and I can safely say that these have been some of the most developing years of my life so far. Several people have contributed to this fact, and perhaps the most significant contribution is due to my supervisor, Tünde Fülöp, who initially opened the door and brought me into the world of plasma physics. I still find myself amazed by her remarkable diligence, which has ensured that she can always find time to help and discuss with her students. I am also very grateful to my co-supervisor István Pusztai who, whenever any difficult question arises—be it career or physics related—is standing by to provide comfort and advice.

The years of SOFT development have required hard work, but they have also brought much joy. The countless discussions and close collaboration with Ola Embréus is unquestionably the best example of this. Ola has been a strong influence on both me and my work, in addition to making work all the more joyful. Another highlight of SOFT development has been interacting with Alex Tinguely, whose impressive work ethics and many emails are the source of some of the most important results of this thesis.

My gratitude extends also to those who have read and commented on the draft of this thesis. They include the people already mentioned, as well as Gergely Papp, Linnea Hesslow and Sarah Newton.

Finally, I want to thank the members of the Plasma Theory group, old as well as new, for creating a first-class work environment. I am very much looking forward to the many coffee breaks and discussions that lie ahead of us!

Mathias Hoppe, Göteborg, January 2019

x

Chapter 1

Introduction

It has been established scientifically, well beyond all reasonable doubt, that global climate change is one of the most immediate and severe threats to our planet and humanity as a whole [1]. To counter this threat, we must drastically reduce our use of fossil fuels, which are among the primary sources of greenhouse gases. Replacing coal, oil and natural gas is however not a simple matter, as we have grown far too used to the large amount and stable supply of energy they provide.

One alternative energy source that could provide both the stability and vast amount of energy that fossil fuels give us today is *nuclear fusion*. In fusion, the nuclei of two light atoms (commonly the hydrogen isotopes deuterium and tritium) are combined, i.e. fused together, to produce a heavier nucleus. This process releases a large amount of energy and can be used to generate electricity [2].

While several types of fusion device are under study, the most promising candidate for large-scale fusion production is currently the torus-shaped, so-called *tokamak*, illustrated in Fig. 1.1. In the tokamak, the fusion fuel is heated to around 150 million Kelvin, at which point electrons and atomic nuclei have separated and constitute a plasma. Using magnetic fields, the plasma can be confined inside the device long enough for fusion reactions to occur. A crucial component of the tokamak, and a main distinguishing feature among magnetic confinement devices, is the large current that runs through the device in the toroidal direction. This generates a magnetic field in the poloidal direction which counteracts the drift motion of the plasma particles that would otherwise rapidly force them out of the device.
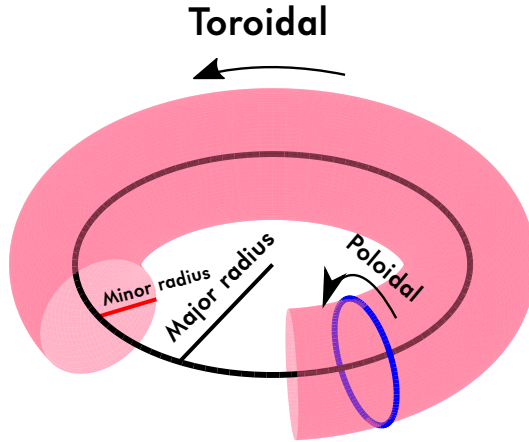
Figure 1.1: Illustration of a tokamak coordinate system.

Under certain circumstances, instabilities can arise in the tokamak that rapidly cool the plasma and cause the toroidal current to dissipate [3–5]. This, in turn, induces a strong electric field that can accelerate particles and which, due to a fundamental property of plasmas, can give rise to a phenomenon known as *runaway electrons*. This phenomenon occurs since, in a plasma, the friction force experienced in collisions with other plasma particles decreases as a particle moves faster. If an accelerating electric field is strong enough it can therefore lead to a runaway of the particle energy. In particular electrons are prone to being accelerated to high energies, due to their light mass [6].

Today, electron runaway is considered to be one of the primary threats facing commercial tokamak fusion reactors, and it is therefore of utmost importance to understand how runaway electrons are generated and how they can be mitigated. A thorough understanding of runaway electrons requires the development of theoretical models, which must then be tested in experiments. The connection between theory and experiment is however not always straightforward, as theory is usually concerned with the detailed dynamics of particles, whereas experiments produce diagnostic signals that, in most cases, depend only indirectly on the particle dynamics. The aim of this thesis is to bridge the divide between runaway electron theory and experiment, by presenting a synthetic radiation diagnostic that can be used to predict what diagnostic signal a given population of runaway electrons will give rise to. Before

Figure 1.2: Illustration of a particle orbit in a magnetic field. The orbit takes the form of a helix that is wrapped around magnetic field lines, due to the Lorentz force. Often, one is not interested in the gyrating motion around magnetic field lines, and instead studies the *guiding-center* of the orbit (dashed line).

presenting the model in detail, we will first review the basic theory of runaway electrons and their radiation.

1.1 Electron dynamics in tokamaks

The motion of individual electrons in a tokamak is primarily governed by the Lorentz force [7],

$$\boldsymbol{F} = -e\left(\boldsymbol{E} + \boldsymbol{v} \times \boldsymbol{B}\right), \qquad (1.1)$$

where e is the elementary charge, $\boldsymbol{v}$ is the particle velocity, and $\boldsymbol{E}$ and $\boldsymbol{B}$ are the electric and magnetic fields acting on the particle. The second term in this equation causes the particle to move in a helical orbit, approximately around magnetic field lines, as illustrated in Fig. 1.2. This allows us to decompose the motion of the particle into two parts: rapid gyro motion approximately perpendicular to the magnetic field, and smoother "average" motion of the particle, approximately along the magnetic field (indicated by the dashed line in Fig. 1.2). This latter part of the motion is often referred to as the *guiding-center* motion of the particle, and the mathematical theory concerned with the decomposition of motion just described is called *guiding-center theory* [8]. The key assumption of guiding-center theory is that the magnetic field varies slowly during one gyration of the particle orbit, which allows equations of motion for the guiding-center to be given as an expansion series using the radius of the gyro motion (known as the gyro or Larmor radius) as the expansion parameter. In this thesis, we often (but not always!) consider the guiding-center theory only to zeroth-order, in which guiding-centers exactly follow magnetic field lines. In the standard guiding-center theory, which is more widely used, the first order

terms are kept, and the guiding-center deviates slightly from the field lines, a phenomenon known as *drifting*.

To study the dynamics of electrons in a plasma, the equations of motion could be solved for each particle in the plasma with the help of Eq. (1.1). This approach soon proves computationally infeasible however, as the density of particles in a typical tokamak plasma is of the order $\sim 10^{20}\,\mathrm{m}^{-3}$. Instead, a statistical approach can be taken whereby the probability distribution for finding an electron in a given state is propagated in time. This probability distribution is known as the *distribution function* and is usually denoted $f(\boldsymbol{x}, \boldsymbol{p}, t)$. It is typically normalised such that an integration over all coordinates of phase space yields the total number of electrons in the plasma.

The distribution function plays a central role in this thesis and appears as a key component in the radiation diagnostic integral presented in Chapter 2 and Paper A. Despite this, it should be pointed out that the theory we present here does not evolve the distribution function in time, but rather relies on external methods for doing so. When the distribution of runaway electrons is needed, we either rely on previous analytical results [9] or the numerical code CODE [10, 11].

1.2 Runaway electrons

The mechanism behind electron runaway in plasmas has been known since the early 1900's [12], and its first theoretical description is often credited to Dreicer [13, 14]. He showed that since the friction force experienced by a particle moving faster than the thermal speed (i.e. the average speed of particles at the given temperature) is $\propto 1/v^2$, where v denotes the speed of the particle under consideration, an applied electric field would yield a net acceleration of all particles faster than some threshold speed v_c. In the absence of any other decelerating forces, the particle would accelerate indefinitely and approach the speed of light, a process commonly known as *runaway*. The theory of electron runaway was later extended to relativistic particles [15], and it was shown that special relativity sets a lower limit E_c on the applied electric field for any runaway electrons to be generated at all. Due to its decisive role in the runaway process, this critical electric field has since been the subject of much research, which has resulted in refined theoretical predictions that account for effects such as radiation reaction losses [16] and par-

tial ionisation of the background plasma [17], as well as experimental measurements of the limit [18–20].

While runaway electrons have now been identified in a variety of plasmas, including solar flares [21] and thunderstorms [22, 23], their presence in tokamak plasmas [24] is of particular concern to the magnetic fusion research community. If control is lost over a beam of runaway electrons that is carrying a significant current, the runaway beam can deposit a large amount of energy in a localised region on the device wall. This can lead to severe damage to the wall, requiring repairs that may be both costly and lengthy.

What puts the tokamak at a particularly high risk of runaway electron damage is the fact that it occasionally experiences instabilities leading to *disruptions* which abruptly cool the plasma and cause the plasma current to dissipate [25–27]. As the plasma current drops, a strong toroidal electric field is induced which can accelerate electrons and cause them to become runaways.

Runaway generation is further exacerbated during disruptions by a mechanism known as *hot-tail* generation [28–32]. When the plasma temperature drops, it takes some time for the electron distribution to equilibrate at the new temperature. Due to the non-monotonic nature of the collisional friction force previously described, the fastest electrons tend to take the longest to slow down, and as a result they form a "tail" in the super-thermal part of the electron energy distribution. This hot tail of electrons is particularly prone to being accelerated by the induced electric field and hence producing runaway electrons.

The hot-tail generation mechanism is however not the sole reason that runaway electrons are of particular concern in tokamaks. In addition to being generated through continuous electric field acceleration, often called *primary generation*, runaway electrons can also be generated through a mechanism known as *avalanche* or *secondary generation* [33–36]. In the avalanche generation process, a highly energetic electron collides with a thermal electron and imparts a significant amount of energy to it, turning the thermal electron into a runaway electron while retaining enough energy to remain a runaway electron itself. Although this requires an existing seed of runaway electrons, once present, the seed multiplies exponentially. Through this mechanism, it is therefore possible for the entire plasma current to be converted to runaway electrons in the presence of even a weak electric field, as long as it is stronger than E_c. In a tokamak with a large plasma current that can be poten-

tially converted to runaway electrons, such as ITER, the combination of hot-tail and avalanche can therefore have devastating consequences.

Due to the severity of the runaway problem in tokamaks, several mitigation schemes have been developed. The most promising schemes at present are all based on injection of heavy impurities into the plasma, either in the form of gas or solid pellets [37]. The heavy ions act to increase the friction force experienced by the runaway electrons and increase the dissipation of the runaway energy through bremsstrahlung emission.
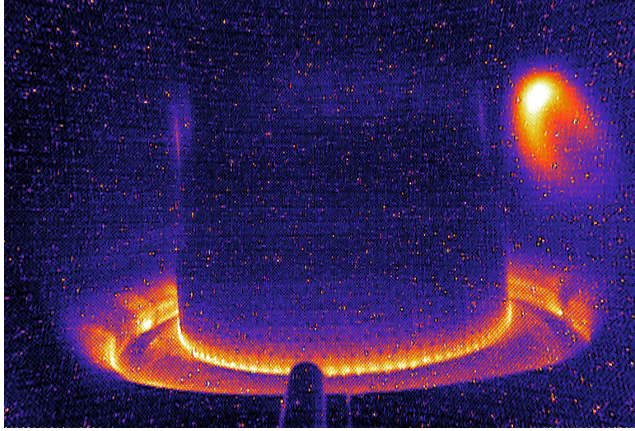
1.3 Radiation from runaway electrons

Relativistic runaway electrons primarily emit two types of radiation: bremsstrahlung (from collisions with the background plasma) and synchrotron radiation (from motion around magnetic field lines). The emitted radiation serves both as an important energy loss mechanism [16, 38–41] and can be used to diagnose many aspects of runaway electron dynamics. We will focus on the latter point in this thesis.

Since the pioneering measurements of synchrotron radiation from relativistic runaway electrons on the TEXTOR tokamak in 1990 [42], synchrotron radiation has become a standard diagnostic in runaway electron experiments. Today, many tokamaks are equipped with some form of diagnostic that is able to measure synchrotron radiation, and measurements have been performed on several of them, including Alcator C-Mod (see Papers A, B and D), ASDEX Upgrade [43], COMPASS [44], DIII-D [20, 45–48], EAST [49–51], FTU [52], HL-2A [53], HT-7 [54], J-TEXT [55], KSTAR [56], TCV [43] and TEXTOR [42, 57–64]. Typically, a significant fraction of synchrotron radiation is emitted at visible or near-infrared (IR) wavelengths, which allows common visible-light cameras and spectrometers to serve as synchrotron diagnostics. It is also possible to use the total amount of emitted synchrotron radiation to indicate the presence of runaway electrons or to estimate runaway energy loss rates. To interpret measurements, several models have previously been developed and applied [65–70], allowing pitch angle, energy and position to be inferred from camera images and spectra.

Bremsstrahlung has also been used to diagnose runaway electrons for several decades [71, 72] due to the fact that the runaways emit hard X-rays (HXR) which can be distinguished from the lower energy soft X-ray (SXR) bremsstrahlung emitted by the rest of the plasma. For runaway

Figure 1.3: A false-coloured, visible-light, synchrotron image taken in the Alcator C-Mod tokamak during discharge 1140403026. The bright spot on the right is synchrotron radiation from runaway electrons. (Photograph courtesy of R. A. Tinguely and R. S. Granetz).

electrons, typical photon energies range from a few tens of keV to several MeV. HXR counters and spectrometers are widely used today to indicate the presence of runaway electrons in experiments, and runaway energy distribution functions have been constrained from measurements of bremsstrahlung spectra [47, 73, 74]. At the DIII-D tokamak, a HXR camera called the "Gamma Ray Imager" (GRI) [75, 76] was recently installed with the purpose of producing energy-resolved bremsstrahlung images.

Common to both bremsstrahlung and synchrotron radiation from relativistic electrons is that the relativistic beaming effect causes the radiation to be emitted almost entirely along each electron's velocity vector [77]. Only those electrons travelling towards the observer can therefore be detected, placing a constraint that relates points of momentum space to points in real space. The result is that camera images of the directed radiation show "spots" of radiation, such as in Fig. 1.3. The shape of the spot depends sensitively on both the energy and pitch angle of the runaways, and can also reveal their radial distribution.

Although both spectra and camera images are of interest in experiments, this thesis is focused primarily on the latter. The reason for this is that much of the previous work done on the topic has examined bremsstrahlung and synchrotron spectra in great detail, while neglecting the spatial structure of the radiation, which becomes especially appar-

7

ent in camera images. In this thesis we explore the previously neglected effects, which is therefore best done using images.

1.4 Thesis outline

Chapter 2 introduces the theory which underlies the rest of this thesis. The radiation diagnostic integral is presented in its most general form, as well as the conceptually and practically important cone approximation. Another important concept for our analysis is the diagnostic response function, which is also introduced here. In Chapter 3, a dedicated and deeper analysis of the diagnostic response function is conducted. We review the impact of what can be called geometric effects on the response function, and compare to models that neglect such effects. This naturally leads to a discussion about how the shape of the distribution affects the diagnostic signal. A highlight of the main results of the appended papers is then given in Chapter 4, where we also discuss possible areas of improvement and further work.

Chapter 2

Radiation diagnostic theory

Ever since the first experimental measurements of radiation from relativistic runaway electrons were conducted [78], models for the radiation have been developed [79]. In tokamaks, the first use of synchrotron radiation as a diagnostic for relativistic runaway electrons was presented in Ref. [42]. While early attempts to model the runaway synchrotron radiation in tokamaks focused on estimating the curvature radius appearing as a parameter in the synchrotron spectrum, as well as the pitch angle of the runaways from the synchrotron spot shape [42], subsequent efforts incorporated elements of the magnetic field geometry and runaway distribution function into the models [66, 80]. On the bremsstrahlung side, a more sophisticated approach was taken, resulting in the development of the synthetic bremsstrahlung diagnostic R5-X2 [72]. In contrast to the models used for synchrotron radiation, R5-X2 evaluates an integral over the plasma volume, momentum space and detector field-of-view, and is able to take the magnetic field geometry into account. Only recently, the synthetic diagnostic approach has also found its way into models of synchrotron radiation, manifested in the synchrotron radiation module of the orbit code KORC [70, 81], and the *Synchrotron-detecting Orbit Following Toolkit* (SOFT) presented in Paper A.

This chapter gives a brief introduction to the synthetic radiation diagnostic model derived in Paper A, which differs in many aspects from other models. One of the strengths of the model in Paper A is that it permits the use of a simplified emission model, referred to as the *cone model*, which not only reduces the computational demands, but also gives some physical insight that is hard to come by using more advanced emission models.
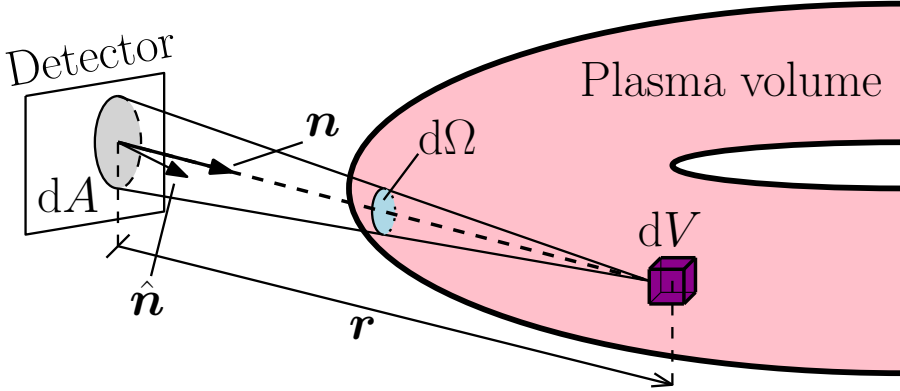
Figure 2.1: Illustration of the synthetic diagnostic setup described in Section 2.1. The synthetic diagnostic sums up the radiation coming from all volume elements $\mathrm{d}V$ in the plasma

2.1 Radiation diagnostic formulation

The function of a general radiation diagnostic, measuring some quantity I (which can be, for example, radiated power or number of photons), is illustrated in Fig. 2.1. Assuming that the plasma is optically thin to the radiation, we can write the total received radiation from the plasma volume V, along the line-of-sight specified by the unit vector $\boldsymbol{n}$, as

$$I_{\boldsymbol{n}}(\boldsymbol{x}_0, t) = \int_V \delta^2 \left(\frac{\boldsymbol{r}}{r} - \boldsymbol{n} \right) \frac{\mathrm{d}I(\boldsymbol{x}, \boldsymbol{n}, t)}{\mathrm{d}V} \, \mathrm{d}V, \tag{2.1}$$

where $\delta^2(\boldsymbol{x})$ is a two-dimensional Dirac delta function, and $\boldsymbol{r} = \boldsymbol{x}_0 - \boldsymbol{x}$ is a vector between the detector at $\boldsymbol{x}_0$ and the point $\boldsymbol{x}$ of space where radiation originates.

Typically, we are interested in the radiation seen in the entire field-of-view of the detector, or the field-of-view corresponding to a particular camera pixel, and then we must integrate over the set $\Omega_{\boldsymbol{n}}$ of all line-of-sight directions $\boldsymbol{n}$ in the field-of-view. If we integrate Eq. (2.1) over $\Omega_{\boldsymbol{n}}$ we find that

$$I = \int I_{\boldsymbol{n}} \, \mathrm{d}\Omega_{\boldsymbol{n}} = \int_V \Theta \left(\frac{\boldsymbol{r}}{r} \right) \frac{\mathrm{d}I(\boldsymbol{x}, \boldsymbol{r}, t)}{\mathrm{d}V} \mathrm{d}V, \tag{2.2}$$

where the delta function has substituted $\boldsymbol{n}$ for $\boldsymbol{r}/r$ and given rise to a function $\Theta(\boldsymbol{r}/r)$ that is one when $\boldsymbol{r}/r \in \Omega_{\boldsymbol{n}}$, and zero otherwise. In other words, the integration over $\Omega_{\boldsymbol{n}}$ makes explicit the fact that only

particles situated in the detector's field-of-view can contribute to the measurement.

The amount of radiation received from an infinitesimal volume element $\mathrm{d}V$ in the plasma, by a detector with area A, occupying a solid angle Ω as seen from the emitter, is

$$\frac{\mathrm{d}I}{\mathrm{d}V} = \int_{\Omega} \frac{\mathrm{d}^2 I}{\mathrm{d}V \mathrm{d}\Omega} \, \mathrm{d}\Omega. \tag{2.3a}$$

Often, it is more convenient to express Eq. (2.3a) as an integral over the detector surface instead of the solid angle subtended by the detector. The surface area taken up by the solid angle $\mathrm{d}\Omega$ a distance r from the emission source is $\mathrm{d}S = r^2 \mathrm{d}\Omega$, and the normal vector of this surface is $\boldsymbol{r}/r$. If we let $\mathrm{d}A$ be the corresponding area of $\mathrm{d}S$ when projected onto the detector surface, with normal $\hat{\boldsymbol{n}}$, then $\mathrm{d}S = (\hat{\boldsymbol{n}} \cdot \boldsymbol{r}/r)\mathrm{d}A$ and

$$\frac{\mathrm{d}I}{\mathrm{d}V} = \int_{A} \frac{\hat{\boldsymbol{n}} \cdot \boldsymbol{r}}{r^3} \frac{\mathrm{d}^2 I}{\mathrm{d}V \mathrm{d}\Omega} \, \mathrm{d}A. \tag{2.3b}$$

The radiation emitted from the volume element $\mathrm{d}V$, into the infinitesimal solid angle $\mathrm{d}\Omega$, is now given by the number of particles in $\mathrm{d}V$, times the amount of radiation emitted by each particle into $\mathrm{d}\Omega$:

$$\frac{\mathrm{d}^2 I}{\mathrm{d}V \mathrm{d}\Omega} = \int \frac{\mathrm{d}I(\boldsymbol{x}, \boldsymbol{p}, \boldsymbol{r})}{\mathrm{d}\Omega} f(\boldsymbol{x}, \boldsymbol{p}) \, \mathrm{d}\boldsymbol{p}. \tag{2.4}$$

Here, $f(\boldsymbol{x}, \boldsymbol{p})$ is the electron distribution function and $\mathrm{d}I/\mathrm{d}\Omega$ describes the angular distribution of radiation emitted by each particle. Depending on which type of radiation we would like to model, we pick a suitable form for the angular distribution of radiation. For synchrotron radiation we would take it to be the total received power per unit solid angle $\mathrm{d}P/\mathrm{d}\Omega$, while for bremsstrahlung we would take it to be the differential cross-section of photon production, multiplied by the electron speed and local plasma density, to get the number of detected photons.

For completeness, we also give the combined form of the radiation diagnostic integral. Combining Eqs. (2.1)-(2.4), we obtain

$$I = \iiint \Theta \left(\frac{\boldsymbol{r}}{r} \right) \frac{\boldsymbol{r} \cdot \hat{\boldsymbol{n}}}{r^3} \frac{\mathrm{d}I(\boldsymbol{x}, \boldsymbol{p}, \boldsymbol{r})}{\mathrm{d}\Omega} f(\boldsymbol{x}, \boldsymbol{p}) \, \mathrm{d}\boldsymbol{p} \, \mathrm{d}V \, \mathrm{d}A. \tag{2.5}$$

This is, in essence, the integral that the simulation tool SOFT evaluates. It serves as the starting point of the theory developed in Paper A, which transforms the set of coordinates used in Eq. (2.5) to a set more suitable for integrating along runaway orbits. The details and implications of this coordinate system is the topic of the next section.

(a) Uniform   (b) Full-orbit   (c) Guiding-center
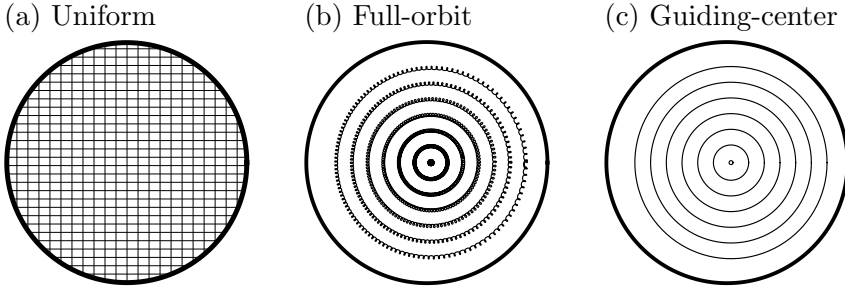
Figure 2.2: Sketch of how the plasma can be parameterised in a synthetic diagnostic. A direct/uniform discretisation of phase space would look something like (a), whereas (b) represents phase space parameterised by particle orbits. In SOFT and R5-X2, guiding-center orbits are however used to parameterise phase-space, as in (c).

2.2   Phase space parameterisation

We now have a general model of a radiation diagnostic, embodied in Eq. (2.5), which could in principle be implemented in a simulation code as it stands. In practice, however, the physics of the problem allows for a range of simplifications that reduce computational costs. A first such simplification is to discretise phase space in terms of orbits rather than, for example, uniformly in Cartesian coordinates (i.e. by representing the phase-space integral as a Riemann sum) as is schematically illustrated in Fig. 2.2. The main benefit of this approach is that the value of the distribution function need only be known at one point along the orbit— Liouville's theorem then ensures that we can deduce the value of the distribution function at every other point along the orbit, under the additional assumption that collisions and other dissipative effects (such as radiation emission) are negligible on the orbit time-scale.

    The most accurate way of utilising orbits for discretising phase-space is to use particle orbits, often referred to as the *full-orbit* approach. This would correspond to the parameterisation in Fig. 2.2(b) and is effectively the parameterisation used for example in KORC [70, 81]. While this ensures that all features of the orbits are accurately captured, it is still a computationally expensive and numerically challenging approach.

    An alternative approach, which is taken by both R5-X2 and SOFT, is to parameterise phase space using computationally cheaper guiding-center orbits [8, 82, 83]. In this approach, which is schematically illustrated in Fig. 2.2(c), the rapid gyro-motion is explicitly separated from

the much smoother guiding-center motion of the particle. The benefits of this are more than just obtaining smoother orbits, as it allows radiation formulas to be integrated analytically over the gyro angle, reducing the dimensionality of the integral Eq. (2.5). Similar coordinate systems are also used in 3D kinetic solvers such as CQL3D [28, 84, 85] and LUKE [86, 87]. The primary drawback is that the particle orbits are approximated with guiding-center theory, which assumes that the Larmor radius $p_\perp/eB$ (with $p_\perp$ the particle's momentum perpendicular to the magnetic field with magnitude B, and e the absolute value of the particle's charge) is much smaller than the length scales of the magnetic-field variations. The guiding-center theory will therefore break down when the runaway energy becomes very large, at which point full-orbit simulations become necessary.

The use of guiding-center orbits to parameterise phase-space also provides one additional benefit compared to the full-orbit approach. Since full-orbit calculations are relatively expensive to conduct, there is currently no feasible way of computing the full-orbit electron distribution function. Instead we must use tools such as the aforementioned kinetic solvers CQL3D and LUKE—which assume that either zeroth or first order guiding-center theory holds—or kinetic solvers such as CODE [10, 11] which altogether neglect the spatial dynamics. While it may be possible to combine these approaches, i.e. running a full-orbit simulation of the radiation with a distribution function obtained using first-order guiding-center theory, one must be cautious when interpreting the subsequent results. The calculation will only be as accurate as its least accurate component, meaning that using a distribution function computed using first-order guiding-center theory together with a full-orbit model for the radiation will *not* accurately capture full-orbit effects.

The coordinate system used in SOFT consists of the following six guiding-center coordinates:

ρ = Maximum major radius visited by guiding-center along orbit,

τ = Time coordinate along guiding-center trajectory
(at $\tau = 0$, the guiding-center is located at ρ),

$\phi^{(0)}$ = Toroidal angle of the guiding-center at $\tau = 0$,

$p_\parallel^{(0)}$ = Guiding-center parallel momentum at $\tau = 0$,

$p_\perp^{(0)}$ = Guiding-center perpendicular momentum at $\tau = 0$,

ζ = Gyro angle.

(2.6)

The first three coordinates parameterise the position of the guiding-center along the orbit; the guiding-center starts out at its outermost radial point ρ, at some toroidal angle $\phi^{(0)}$, and then follows a path parameterised by the time τ. The next three coordinates span momentum-space, and while the choice of $p_\parallel^{(0)}$ and $p_\perp^{(0)}$ is often convenient for runaway problems, it is not required and can be replaced by any equivalent set of coordinates (e.g. momentum and pitch angle $\theta_{\mathrm{p}} = \arctan p_\perp / p_\parallel$). The main point is that ζ must always be chosen as the third coordinate, since this is required by the guiding-center transformation.

As previously mentioned, with an orbit parameterisation of phase space, Liouville's theorem allows us to determine the value of the distribution function at any point along the orbit. Specifically, Liouville's theorem states that the distribution function satisfies $\mathrm{d}f/\mathrm{d}\tau = 0$, i.e. is independent of τ, assuming that dissipative effects and time variations in plasma and magnetic geometry parameters are negligible on the orbit time scale. Moreover, it can be shown that f will be independent of the gyro angle to the order of interest [6], and since we assume the tokamak to be axisymmetric, the distribution function must be independent of $\phi^{(0)}$. The only parameters that remain for the distribution function to depend on are therefore ρ, $p_\parallel^{(0)}$ and $p_\perp^{(0)}$.

Returning to Eq. (2.5), we now consider the radiation diagnostic integral from a different perspective. Since the input signal—the distribution function—only depends on three parameters, we can separate the integrand of Eq. (2.5) into two parts. These are the distribution function $f(\rho, p_\parallel^{(0)}, p_\perp^{(0)})$, and a function $G(\rho, p_\parallel^{(0)}, p_\perp^{(0)})$ which consists of the other factors of the integrand in Eq. (2.5), including the integrals over detector surface, toroidal angle, orbit time and gyro angle. We may

then write the detected radiation as

$$I = \iiint G\big(\rho, p_\parallel^{(0)}, p_\perp^{(0)}\big)\, f\big(\rho, p_\parallel^{(0)}, p_\perp^{(0)}\big)\, p_\perp^{(0)}\, \mathrm{d}\rho\, \mathrm{d}p_\parallel^{(0)}\, \mathrm{d}p_\perp^{(0)}, \qquad (2.7)$$

making sure to include the momentum space Jacobian determinant $p_\perp^{(0)}$. The function G is the response function of the diagnostic setup, representing essentially the orbit averaged received emission from the particles. This form of the synthetic diagnostic integral is often convenient, as the linear relation between I and f enables the discretised integral to be represented as a matrix multiplication. By pre-computing G, it is possible to quickly compute I from an arbitrary distribution function f, something that was utilised for fitting the radial density of electrons to a set of synchrotron images from Alcator C-Mod in Paper D.

The response function G is difficult to characterise in general, since it not only depends on the three phase space parameters, but also on the instantaneous magnetic geometry and detector setup. At the same time, it is arguably the single most important object to study for any diagnostic setup. In Chapter 3 we will take a closer look at the properties of a particular response function that will serve as a representative example.

2.3 Cone approximation

One particular form of the radiation function $\mathrm{d}I/\mathrm{d}\Omega$ in Eq. (2.4) is found to be especially useful for the radiation emitted by relativistic runaway electrons. As illustrated in Fig. 2.3(a), the relativistic beaming effect will direct the radiation along the velocity vector of the particle, with an angular spread that is $\sim \gamma^{-1}$, i.e. the inverse of the relativistic factor of the particle. For highly relativistic particles, which runaways often are, this means that the radiation is emitted almost exclusively along the velocity vector, motivating us to take this as an approximation. The corresponding radiation function is

$$\frac{\mathrm{d}P}{\mathrm{d}\Omega} = \frac{P\left(p_\parallel, p_\perp\right)}{2\pi}\delta\left(\hat{\boldsymbol{v}} \cdot \boldsymbol{n} - 1\right), \qquad (2.8)$$

where $P(p_\parallel, p_\perp)$ represents the total radiation emitted by the particle.

The delta function in Eq. (2.8) ensures that radiation will only be emitted exactly along the direction of motion $\hat{\boldsymbol{v}}$ of the particle, which must be aligned with the line-of-sight $\boldsymbol{n}$ under consideration. After

(a)

(b)
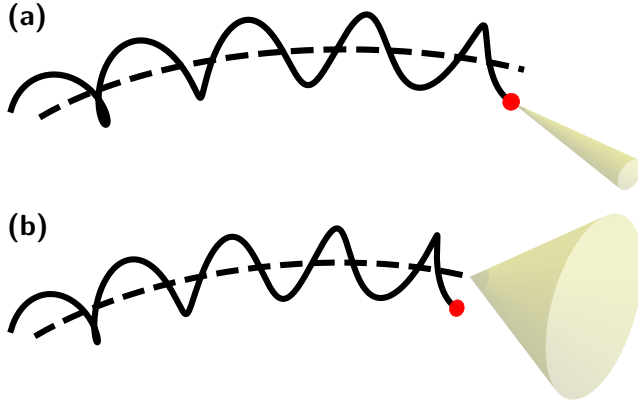
Figure 2.3: Illustration of relativistic (a) *particle* emission versus (b) *guiding-center* emission. Several particles can share the same guiding-center, and when the radiation of all of those particles is considered, that guiding-center can be considered as emitting radiation in a larger cone with opening angle θ_{p} (the pitch angle of the particles).

applying a guiding-center transformation to Eq. (2.8) and integrating it over the gyro angle, a corresponding expression is obtained that describes the emission of the guiding-center:

$$\int_0^{2\pi} \frac{\mathrm{d}P}{\mathrm{d}\Omega}\,\mathrm{d}\zeta = P\left(p_\parallel, p_\perp\right)\,\delta\left(\hat{\boldsymbol{V}}\cdot\boldsymbol{n} - \cos\theta_{\mathrm{p}}\right), \qquad (2.9)$$

where $\hat{\boldsymbol{V}}$ denotes a unit vector in the direction of motion of the guiding-center and $\theta_{\mathrm{p}} \equiv \arctan(p_\perp/p_\parallel)$ is the pitch angle of the particle. The geometric interpretation of Eq. (2.9) is illustrated in Fig. 2.3(b): the guiding-center emits a circular cone of radiation with half opening angle θ_{p}, centered on its direction of motion $\hat{\boldsymbol{V}}$; hence the name "cone approximation."

Equation (2.9) enables us to build some physical intuition about radiation spot shapes. It asserts that radiation will be detected whenever

$$\hat{\boldsymbol{V}} \cdot \frac{\boldsymbol{x} - \boldsymbol{x}_0}{|\boldsymbol{x} - \boldsymbol{x}_0|} = \cos\theta_{\mathrm{p}}. \qquad (2.10)$$

where $\boldsymbol{x}$ denotes the particle position and $\boldsymbol{x}_0$ the observer's position. To leading order in the guiding-center approximation, $\hat{\boldsymbol{V}}$ is directed along the magnetic field unit vector $\hat{\boldsymbol{b}}$, and hence the cone will sweep past the detector, roughly following magnetic field lines. Whenever the cone overlaps with the detector, radiation is registered.

(a)

(b)
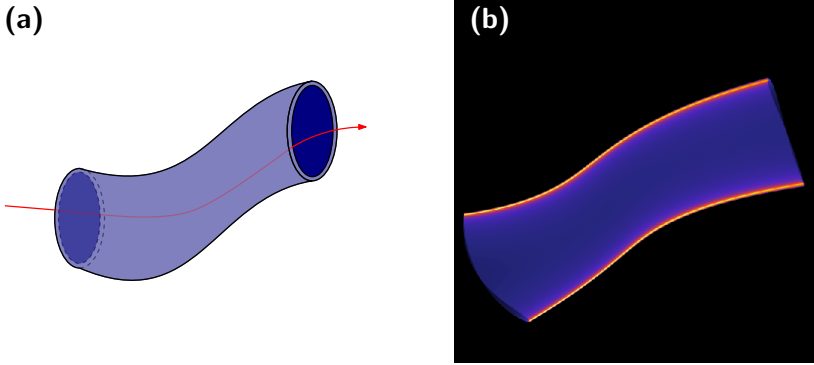
Figure 2.4: (a) Sketch of a surface-of-visibility, emphasising how it takes the shape of a twisted, hollow cylindrical shell. (b) Camera image projection of a simulated SoV. The projection shows how the edges of the observed radiation spot tend to appear brighter to an observer than the rest of the spot. This is due to the cylindrical shape of the SoV which causes lines-of-sight that are tangential to the SoV to receive much more radiation than other lines-of-sight.

If we consider a mono-velocity distribution function, with particles distributed uniformly in ρ, then the points of space satisfying Eq. (2.10) form a surface in space. This surface, which we refer to as a *surface-of-visibility* or SoV, usually takes the shape of a bent and twisted cylinder at small θ_p, and splits into two parts at larger θ_p. Figure 2.4 illustrates the appearance of a hollow, cylinder-shaped SoV. Note that it is only possible to look at the SoV from different perspectives in simulation, due to the dependence on the detector position $\boldsymbol{x}_0$ in Eq. (2.10). Using a camera in an experiment, it is only possible to observe the projection in Fig. 2.4(b).

Although a camera will always see a two-dimensional projection of the SoV, the fact that it has a three-dimensional structure has important consequences for the observed radiation pattern. In particular, this can be observed in Fig. 2.4(b), which shows the projection of a SoV. As is shown there, the upper and lower edges of the projection have brighter colours, corresponding to higher radiation intensity. In these points, the lines-of-sight are tangential to the cylindrical shell that constitutes the SoV, and it can be shown that if the shell is thin, those lines-of-sight will receive the most radiation. From a single point of momentum space—that is, from particles with the same energy and pitch angle—it

is therefore primarily the edges of the SoV that contribute to the total detected radiation.

The basic idea behind the cone approximation—that all radiation is emitted exactly along the velocity vector of the particle—has been known and utilised since the early days of runaway synchrotron measurements. It has served as, arguably, the most important approximation for synchrotron radiation, and is the source of many of the fundamental results within the topic [65, 66, 69]. In simulations, use of the cone approximation can substantially reduce computation times, while maintaining good agreement with more complete models of the radiation, as we demonstrate in Paper A. For this reason, the cone approximation has been used in most simulations of this thesis.

Chapter 3

Properties of the diagnostic response function

The synthetic diagnostic integral (2.5) can be written as an integral over the product of the distribution function f ("the input signal") and the diagnostic response function G. This form of the integral has both practical and theoretical benefits. One example of the practical benefits is given in Paper D, where the ability to approximate this integral transformation with a matrix multiplication and quickly evaluate it was utilised to fit a radial distribution function to a set of experimental synchrotron images.

The theoretical significance of the response function stems from the fact that it maps points of phase-space to diagnostic signals, and hence reveals which parts of phase-space the diagnostic is particularly sensitive to. It can also be used to provide insight into how the radiation spot shape is influenced by various features in the distribution function.

This chapter is dedicated to the diagnostic response function, and the central question we address is: how do radiation measurements depend on the magnetic field geometry, detector set-up and runaway properties? This question is advantageously answered by studying radiation images of mono-energetic and mono pitch-angle populations of runaway electrons. Such images are highly sensitive to all the aforementioned parameters, and we therefore begin the chapter with an in-depth analysis of them. We next proceed to consider what happens when the electron distribution function is taken into account. As we shall see, one point of momentum-space will dominate the detected radiation, and the location of this point is a characteristic of the diagnostic response function.

Finally, we isolate the geometric effects in the response function and interpret them using the surface-of-visibility concept resulting from the cone approximation.

3.1 Radiation spot shape taxonomy

Directed radiation such as bremsstrahlung and synchrotron radiation gives rise to radiation spots that can be observed using cameras. What shape the radiation spot takes depends on several parameters: the magnetic field geometry, detector properties and runaway distribution. While the relation between the radiation spot shape and the runaway pitch angle was identified already in Ref. [42], the first model for the radiation spot shape taking the magnetic field geometry into account was presented in Ref. [66]. That model accurately describes the shape of the synchrotron radiation spot from runaways with small pitch angles, but does not consider the distribution of radiation across the spot. As we show in Papers A and C, the distribution of radiation across the spot can however be of great importance, particularly when the electron distribution function is taken into account and when the magnetic field is weak.

All simulations in this section use the simulation parameters listed in Table 3.1. Since we are concerned with the spot *shapes* due to the directed nature of bremsstrahlung and synchrotron radiation in this section, we primarily consider bremsstrahlung radiation in the cone approximation Eq. (2.9). This is because bremsstrahlung is independent of the magnetic field strength and particle pitch angle, meaning that for a mono-energetic population of runaways, the amount of radiation emitted from different parts of the surface-of-visibility (SoV) will be constant in a homogeneous plasma. Hence, the extent of the SoV and associated shape of the radiation spot become more apparent. In the cases where the magnetic field strength and particle pitch angle strongly influence the synchrotron radiation spot shape, this will be noted. The detector position and viewing direction is indicated in Fig. 3.1.

In most simulations, we use a mono-energetic and mono pitch-angle distribution function, with a uniform radial profile. This distribution function is mathematically described by

$$f(\rho, p, \theta_{\mathrm{p}}) = n_{\mathrm{RE}} \delta\left(p - p_0\right) \delta\left(\theta_{\mathrm{p}} - \theta_{\mathrm{p},0}\right), \tag{3.1}$$

Table 3.1: Simulation parameters used in Section 3.1, unless otherwise noted.

Parameter	Value
Magnetic field strength (on-axis)	2 T
Tokamak major (R_m) / minor (r_m) radius	1.7 m / 0.5 m
Safety factor	Constant, $q = 1$
Detector vertical position	$Z = 0$
Runaway electron energy	$50 m_e c^2 \approx 25$ MeV
Runaway electron pitch angle	0.15 rad
Drift orbits	Neglected

where n_RE is the number of runaway electrons in the simulation, and p_0 and $\theta_\mathrm{p,0}$ denote the momentum and pitch-angle of all the runaways. Note that we suppress the label "(0)" on all parameters in this section for brevity. It is understood that all particle and guiding-center parameters are specified at the point corresponding to the maximum radius visited by the guiding-center along its orbit. Since the number of runaway electrons appears multiplicatively in the distribution function, and hence also in all radiation quantities, we normalise the simulated radiation quantities so that they do not depend on n_RE.

Finally, we also note that all simulations in this section (and also thesis) use zeroth-order guiding-center theory. This means that guiding-center drifts are neglected, since they are formally a first-order effect in the theory. The effects of guiding-center drifts on the radiation are therefore left for future studies.

3.1.1 Magnetic field and detector placement

Both the magnetic field and detector position strongly influence the observed radiation spot shape. For the magnetic field, there is primarily one parameter influencing the spot shape. This parameter is the magnetic field safety factor q, which is a measure of how twisted the tokamak magnetic field is—it is defined as the number of toroidal turns a magnetic field line makes per poloidal turn when traversed. The safety factor determines the inclination of the radiation spot against the horizontal, as illustrated in Fig. 3.2. As a consequence, non-uniform safety factors cause the inclination of the radiation spot to vary, as apparent in Figs. 3.2(c) & (d). In Ref. [51], the inclination angle β_inc between the synchrotron spot and the horizontal was related to the safety factor q,
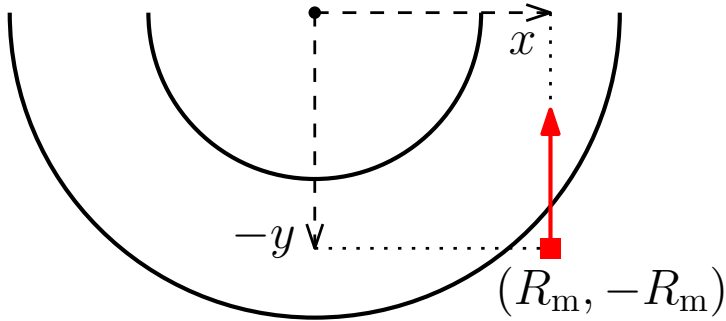
Figure 3.1: Detector setup in the simulations of this section. The detector, denoted by the red square, is located at $(x, y) = (R_{\mathrm{m}}, -R_{\mathrm{m}})$, where R_{m} is the tokamak major radius (see Table 3.1 for numerical value). It is viewing the plasma tangentially, as indicated by the red arrow.
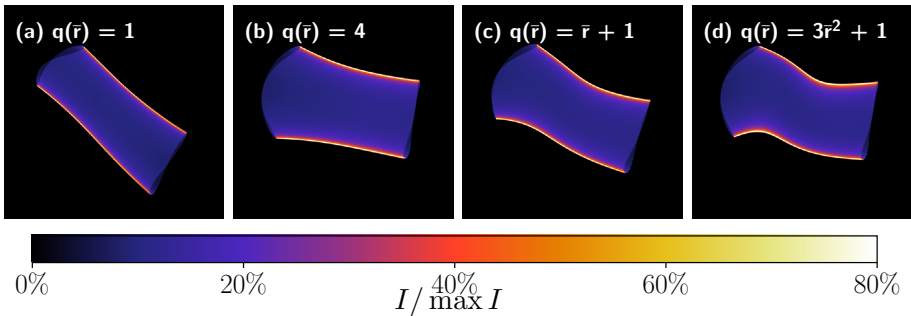
Figure 3.2: Safety factor. Simulated radiation images in four magnetic fields with with different forms for the safety factor $q(\bar{r})$, where $\bar{r}$ is the minor radius normalised to the edge minor radius value. To emphasise the shape of the spot, the colour scale has been chosen such that white corresponds to 80% of the maximum value in any pixel of each image.
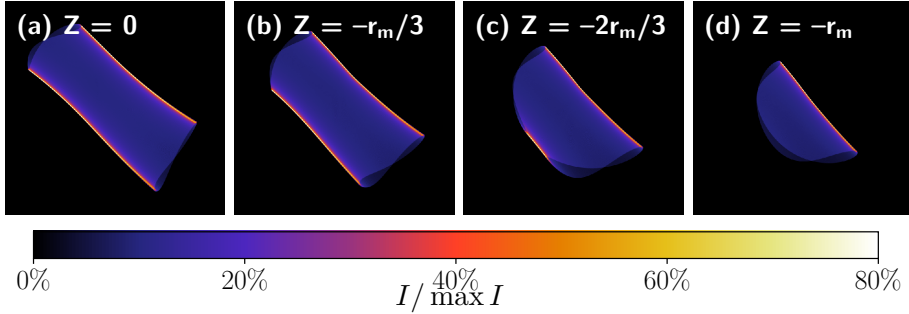
Figure 3.3: Camera vertical placement. Simulated radiation images with the camera located at four different heights. The height $Z = 0$ corresponds to the midplane, and r_{m} denotes the tokamak minor radius. The spot changes similarly when the detector is moved in the opposite vertical direction. To emphasise the shape of the spot, the colour scale is chosen such that white corresponds to 80% of the maximum value in any pixel.

particle-detector distance D and tokamak major radius R_{m} through

$$\tan\beta_{\mathrm{inc}} \approx \frac{D}{q(r)R_{\mathrm{m}}}, \tag{3.2}$$

in the small pitch angle limit. Note that the radial dependence of the safety factor appears here, giving the inclination angle β_{inc} a radial dependence as well.

The magnetic field strength can also indirectly influence the observed radiation spot shape by affecting the amount of radiation emitted at different major radii. Therefore, the effect of magnetic field strength on synchrotron radiation spots can be significant, while it does not affect bremsstrahlung spots. In contrast to the safety factor, the magnetic field strength alone does not alter the geometric condition for when radiation is detected, but rather changes the distribution of radiation intensity across the radiation spot. The intensity distribution however also depends on the detector spectral range and particle momentum, and hence we postpone a discussion of this effect to the next section where the spot shape dependence on particle parameters is discussed.

The detector properties which primarily influence the radiation spot shape are the vertical position of the detector as well as its radial distance to the plasma. Assuming toroidal symmetry, a rotation of the detector in the toroidal direction around the device will not affect the radiation spot shape. Also, since the orientation of the detector only

enters through the geometric factor $\boldsymbol{n} \cdot \hat{\boldsymbol{n}}$ in Eq. (2.5), the orientation will be unimportant as long as the detector is not nearly-perpendicular to the incoming radiation.

Moving the detector along the vertical direction will alter the spot shape in the way shown in Fig. 3.3. Positioning the detector in the midplane will ensure that all particles within the detector field-of-view are visible to the detector, regardless of which flux surface they are on, or what their pitch angles are. If the detector is offset from the midplane, however, particles with small pitch angles located close to the magnetic axis will no longer radiate towards the detector. This is because radiation is emitted with an angle approximately equal to the pitch angle θ_{p} against magnetic field lines. Close to the magnetic axis, magnetic field lines are directed almost entirely in the toroidal direction, meaning that at a distance D from the particle, radiation will be spread $\sim D\theta_{\mathrm{p}}$ from the midplane in both vertical directions. Particles with $\theta_{\mathrm{p}} < Z/D$, located close to the magnetic axis, can therefore not be observed by a detector that is offset from the midplane.

The same argument can be used to reason about how the spot shape is affected when the detector is moved radially away from or towards the plasma. Let Z now instead denote the vertical position of the particle. The largest value of Z such that the particle emits at and is visible to the detector is then $Z \approx D\theta_{\mathrm{p}}$. Since the surface-of-visibility is made up of the particles that emit towards the detector, the vertical extent Δz of the radiation spot must therefore be $\Delta z \propto D\theta_{\mathrm{p}}$. Consequently, the vertical extent of the radiation spot must increase when the detector is moved further away from the plasma, similar to how it is affected by larger particle pitch angles. As is revealed by Eq. (3.2) however, increasing the distance D between the detector and plasma also affects the inclination of the radiation spot relative to the horizontal, since the angles between the lines-of-sight of the detector and the magnetic field change.

3.1.2 Runaway electron properties

Although the magnetic field and detector setup are important for the shape of the radiation spot, the question of primary interest to anyone studying runaway electrons is how the motion and location of the runaways are reflected in the radiation spot. The position and velocity of an electron are fully specified by six parameters, but as discussed in Paper A and Sec. 2.2, these can be reduced to a set of just three param-

eters in a tokamak: the outermost major radius visited by the particle along its orbit ρ, the electron pitch angle θ_p and the electron momentum p. For a given observation setup, the radiation spot characteristics can therefore at most depend on these three parameters.

Pitch angle

The first runaway parameter we consider is the pitch angle, θ_p. The effect of this parameter on the synchrotron spot shape has been discussed extensively in the runaway synchrotron literature [51, 66, 69], precisely because the spot shapes observed in synchrotron images are particularly sensitive to the pitch angle. As is shown in Fig. 3.4, at small pitch angles, the radiation spot is a thin stripe. As the pitch angle grows, the line becomes thicker and the spot grows in size in the vertical direction. The surface-of-visibility, described in Sec. 2.3, roughly takes the shape of a cylinder in Figs. 3.4(a)-(e). At larger pitch angles, the vertical expansion of the spot with pitch angle slows down, and the surface-of-visibility begins to open up into two separate oval surfaces, which is best illustrated by Fig. 3.4(h). At pitch angles beyond $\theta_\mathrm{p} = 0.46\,\mathrm{rad}$, the shapes of the two oval surfaces change little, but rather they move away from each other. In the view from above the tokamak in Fig. 3.5, we see that the two surfaces move in opposite toroidal directions. If this behaviour continues as the pitch angle increases, we would expect one of the surfaces to eventually disappear behind the central column of the tokamak, and this is indeed what happens. In fact, this effect is already visible in Figs. 3.4(h) and 3.5(b), where the central column hides the leftmost part of the smaller spot (corresponding to the upper spot in Fig. 3.5(b)).

Radial location

The next parameter we consider is the maximum radial location of the particle along its orbit. If we only launch particles from a discrete set of radii, we obtain images such as those in Fig. 3.6. Since guiding-centers approximately follow magnetic field lines, each band of radiation in each of Figs. 3.6(a)-(h) originates from particles on the same flux surface. At small pitch angles, each flux surface gives rise to two bands of radiation—one to the right of the magnetic axis, and one to the left. The magnetic axis is located at the point which all bands of radiation appear to encircle, something which is particularly noticeable in
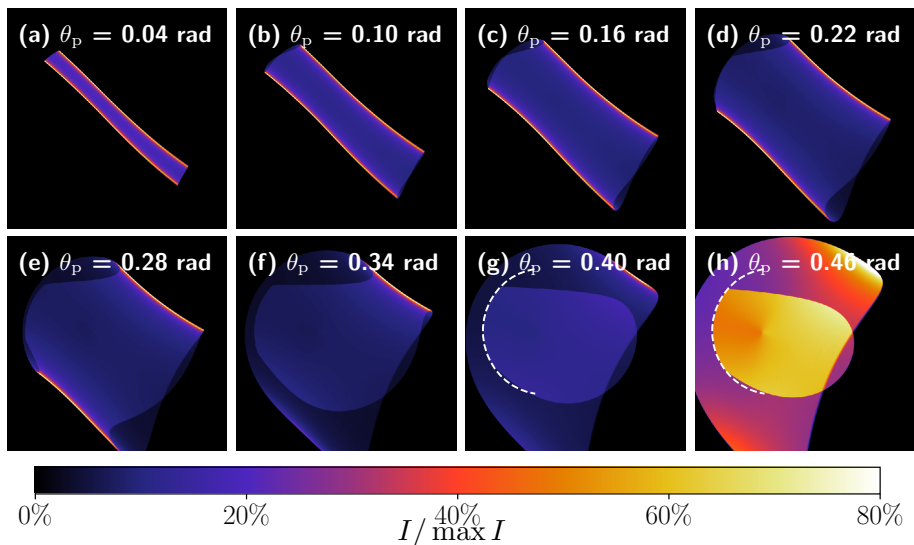
Figure 3.4: Pitch angle. Simulated radiation images showing how the pitch angle affects the radiation spot shape. A larger pitch angle roughly corresponds to a larger vertical extent up until some threshold pitch angle, at which point two separate spots appear and move away from each other. The dashed white lines in (g) and (h) indicate the inner part of the tokamak wall, which blocks out part of the spot in (h). To emphasise the shape of the spot, the colour scale has been chosen such that white corresponds to 80% of the maximum value in any pixel.
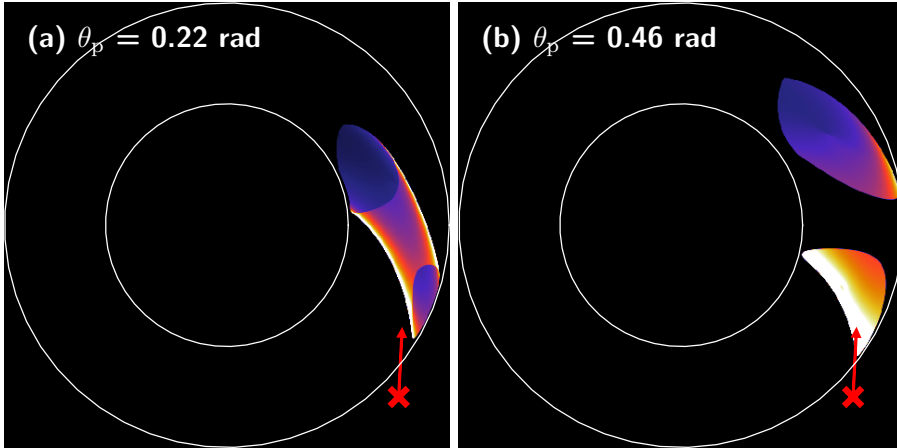
Figure 3.5: Top view of the tokamak, showing the origin of the radiation at (a) $\theta_\mathrm{p} = 0.22\,\mathrm{rad}$ (corresponding to Fig. 3.4(d)) and (b) $\theta_\mathrm{p} = 0.46\,\mathrm{rad}$ (corresponding to Fig. 3.4(h)). The camera position is indicated by the red cross, with its viewing direction designated by the red arrow. At larger pitch angles, the radiation originates from two distinct regions of space which gradually move away from each other, as exemplified in (b).

Figs. 3.6(b)-(d). At larger pitch angles, the bands of radiation split up and join with the corresponding bands at the same radius on the other side of the magnetic axis, as is particularly apparent in the transition between Figs. 3.6(c)-(g).

It is also interesting to note that each pair of radiation bands in Fig. 3.6 corresponds to a single point of the reduced phase space used in SOFT, and described in Sec. 2.2. Any radiation image will therefore be a linear superposition of such bands, each weighted with the corresponding value of the runaway electron distribution function.

Energy

The final phase space parameter which the radiation spot may depend on is the energy of the particle, or equivalently, its momentum p. As it turns out, the radiation spot shape does not in general depend on p in zeroth-order guiding-center theory. This is evidenced by the condition for radiation to reach the detector, Eq. (2.10), which is completely independent of the energy of the particle to zeroth-order.
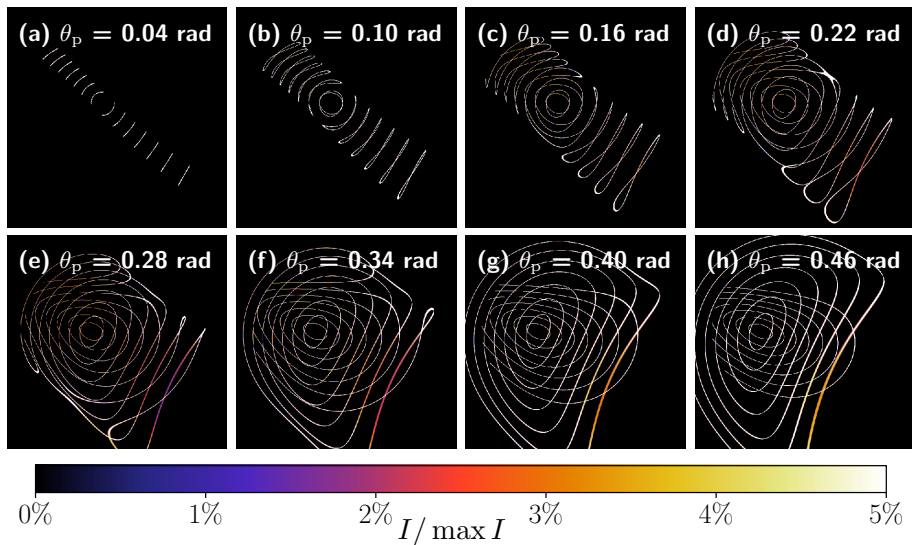
Figure 3.6: Radial location. Each ribbon in these images consists of radiation emitted along an individual guiding-center orbit, approximately corresponding to an individual flux surface. The maximum radii of the ribbons are distributed uniformly between 6 and 48 cm. For comparison with the spots of Fig. 3.4, the pitch angle is varied in each of subfigures (a)-(h). To emphasise the shape of the spot, the colour scale has been chosen such that white corresponds to 5% of the maximum value in any pixel.
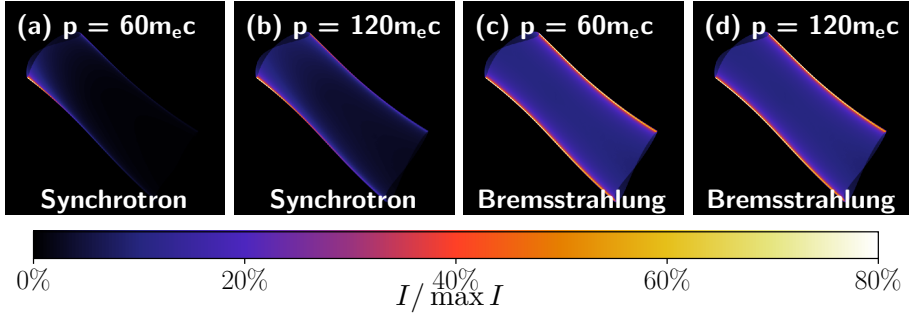
Figure 3.7: Energy. While the overall spot shape is not affected by the energy of the particle, the amount of emitted synchrotron radiation becomes more strongly dependent on magnetic field strength at low energies. Since bremsstrahlung is independent of the magnetic field, its radiation spot shape shows no energy dependence. All images were generated in a magnetic field with $B = 5\,\mathrm{T}$ on-axis. The camera spectral range was $\lambda \in [400, 800]\,\mathrm{nm}$ in the synchrotron case. To emphasise the shape of the spot, the colour scale has been chosen such that white corresponds to 80% of the maximum value in any pixel.

Despite this, the synchrotron spot shape can depend sensitively on the particle energy, something which was noted in Paper C. There, it was shown that due to the strong magnetic field dependence of the synchrotron radiation, combined with the necessarily finite spectral range of all synchrotron cameras, the amount of synchrotron radiation received from a particle at major radius R is

$$P_{\mathrm{synch}} \propto \exp\left[-\left(\frac{R}{R_{\mathrm{c}}}\right)^{3/2}\right]. \tag{3.3}$$

The parameter R_{c} is the *critical radius* and scales as $R_{\mathrm{c}} \propto \sqrt[3]{p^2(1+p^2)}$, where p is normalised to the electron rest mass $m_e c$. It corresponds to the location in the tokamak where, for a given particle energy and pitch angle, the magnetic field is sufficiently strong for the synchrotron radiation spectrum peak to lie within the observing camera's spectral range. Note that Eq. (3.3) is valid only in the limit where the peak of the synchrotron spectrum lies at much longer wavelengths than the camera's spectral range, which is generally the case for visible-light cameras in today's tokamaks.

Due to the strong exponential dependence on R when $R_{\mathrm{c}} \ll R_{\mathrm{m}}$ in Eq. (3.3), synchrotron radiation is often mainly observed on the high field

side in typical scenarios (such as in DIII-D, which has $B = 2.2\,\text{T}$ on-axis under typical operating conditions). The critical radius R_c determines the sensitivity to R—the larger R_c is (corresponding to higher particle energies), the more evenly radiation is distributed between the low- and high field sides of the tokamak. An example of this is shown in Figs. 3.7, where in Fig. 3.7(a) only some radiation is seen on the left side of the image, corresponding to the high field side. At twice the particle energy, in Fig. 3.7, most of the radiation spot is visible. For comparison, the corresponding bremsstrahlung emission is also given in Figs. 3.7(c)-(d), showing that the bremsstrahlung spot shape is independent of p.

The energy dependence can give rise to synchrotron radiation spot shapes that are vastly different from the cylindrical and oval spot shapes exemplified in Figs. 3.2-3.7 when the runaway electron distribution function is taken into account. When the energy of the runaways is low, so that most radiation is emitted at wavelengths that are much longer than the camera's spectral range, contributions from the high field side dominate. When the pitch angle distribution of the particles is taken into consideration, the radiation spot will have a more diffuse pattern. One example of this is shown in Fig. 3.8, where all particles have the same energy, but are distributed in pitch angle according to

$$f(\theta_p) \sim e^{C \cos \theta_p}, \tag{3.4}$$

with $C = 70$. As is shown in Fig. 3.8(a), the synchrotron spot takes a crescent-like shape at low energies, while at higher energies it is possible to identify the spot shape as similar to the cylindrical shape seen in, for example, Fig. 3.4.

It should be mentioned that for bremsstrahlung, even though the energy does not affect the radiation spot shape, the amount of emitted radiation does depend on energy. Since the runaway pitch-angle distribution typically varies with energy, the runaway electron energy distribution will always matter for the resulting radiation spot.

3.2 Dominant particles

In the previous section we considered radiation images from single points of the reduced phase space. This is useful for analysing the dependence of the diagnostic signal on tokamak and runaway parameters, and can help in optimising diagnostic setups. Kinetic theory however predicts runaways to always be widely spread in momentum space, requiring
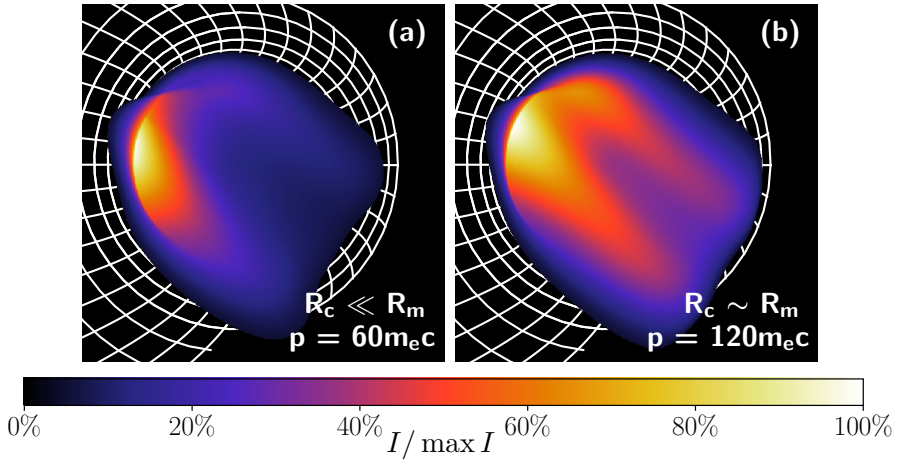
Figure 3.8: Energy. Synchrotron radiation images at two different energies, with particles distributed in pitch angle according to Eq. (3.4). In such scenarios, the synchrotron radiation spot can take a crescent-like spot shape as in (a). At higher energies, such as in (b), the radiation is distributed more evenly across the spot, and it again resembles a cylinder as in for example Fig. 3.4. The white contour lines indicate the location of the circular tokamak wall. Note that the on-axis magnetic field strength was set to $B = 5\,\mathrm{T}$ for this simulation.

Table 3.2: Simulation parameters used to generate Fig. 3.9.

Parameter	Value
Magnetic field strength (on-axis)	5 T
Tokamak major (R_m) / minor (r_m) radius	1.7 m / 0.5 m
Radial distribution of runaways	Uniform, $f(\rho) = \text{const}$
Safety factor	Constant, $q = 1$
Detector vertical position	$Z = 0$
Drift orbits	Neglected

us to take the electron distribution function into account when studying experiments. In a spatially homogeneous plasma where runaway generation is dominated by the avalanche mechanism, the distribution function can be approximated by [9]

$$f(p, \theta_\mathrm{p}) = \frac{C\gamma}{2\pi m_e c \gamma_0 p^2 (1 - e^{-2C\gamma})} \exp\left[-\frac{\gamma}{\gamma_0} - C\gamma \left(1 - \cos\theta_\mathrm{p}\right)\right], \quad (3.5)$$

with p denoting the particle momentum normalised to the electron rest mass $m_e c$, $\gamma = \sqrt{1 + p^2}$, γ_0 the average runaway energy and C a constant that depends on plasma parameters. This distribution function decreases monotonically with energy γ. On the other hand, the amount of emitted radiation typically increases monotonically with the runaway energy, and in the case of synchrotron radiation, also with the pitch angle. The radiation from a runaway population distributed according to Eq. (3.5) should therefore not be dominated by the most common particles in the population, but rather by those particles which collectively contribute the most radiation to the detector. In other words, the detected radiation should be dominated by the point $\boldsymbol{p}$ of momentum space that maximises the product $p_\perp G(\rho, p_\parallel, p_\perp) f(p_\parallel, p_\perp)$, where $G(\rho, p_\parallel, p_\perp)$ is the diagnostic response function as defined by Eq. (2.7), and the factor $p_\perp$ is the momentum-space Jacobian.

Figure 3.9 shows an example distribution function of the form (3.5) with $C = 4$ and $\gamma_0 \approx 51$ in (a), along with the amount of radiation

$$F(p_\parallel, p_\perp) = \int G(\rho, p_\parallel, p_\perp) f(p_\parallel, p_\perp) \, p_\perp \, \mathrm{d}\rho, \quad (3.6)$$

seen by the detector from the runaway population. Figure 3.9(b) uses a response function G corresponding to a bremsstrahlung detector measuring photon energies in the range 511 keV-10 MeV, while Fig. 3.9(c)
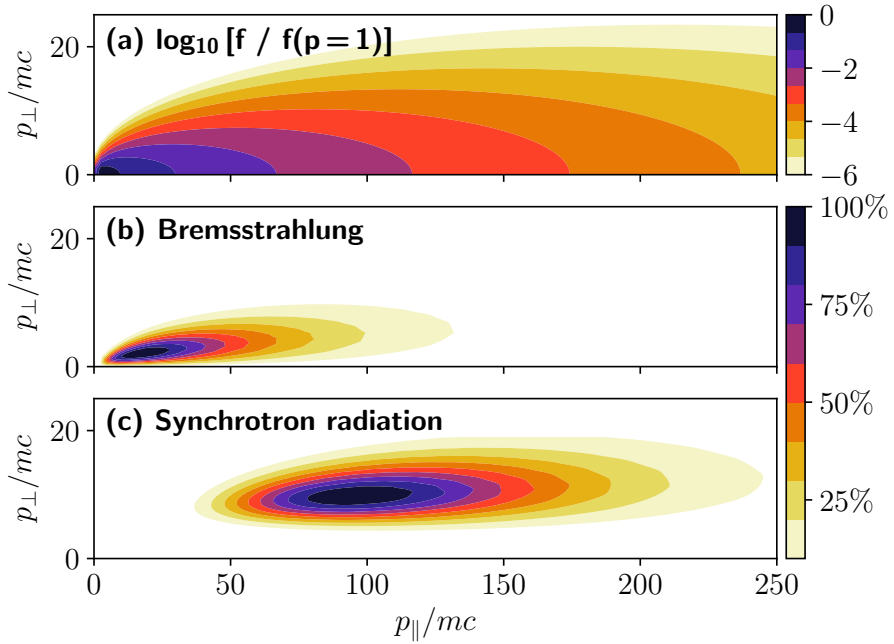
Figure 3.9: (a) A runaway electron distribution function dominated by avalanche generation and contributions to detected (b) bremsstrahlung and (c) synchrotron emission F of Eq. (3.6).

uses that of a synchrotron radiation detector measuring radiation in the wavelength range 400-800 nm. Both response functions have been integrated over all radii. The physical simulation parameters used to generate Fig. 3.9 are presented in Table 3.2.

The maxima in Figs. 3.9(b) and 3.9(c) are examples of what we refer to as the *dominant particles*. Images, spectra and other measured radiation signals from the distribution in Fig. 3.9(a) will have features reminiscent of signals originating purely from the dominant point of momentum space. Often, it is therefore sufficient to assume that all runaways have the same energy and pitch angle to reproduce the main features of a diagnostic signal. The particular energy and pitch angle that best matches the signal is in general, however, not representative of the actual runaway electron population. It is merely the point of momentum space that is best resolved by the diagnostic.

The location of the dominant particle in momentum space depends on both the runaway electron distribution function and the diagnostic response function. This means that different types of radiation will be associated with different dominant particles, as evidenced in Figs. 3.9. It however also means that the same type of radiation, from the same distribution function, measured at a different wavelength, or originating from a different position of the device, will be associated with a different dominant particle. Therefore, multiple detectors viewing the runaways from different positions and at different radiation wavelengths may be able to probe complementary parts of the distribution function and provide a more complete picture of the runaway dynamics.

3.3 Geometric effects

The location of the dominant particle, introduced in the previous section, in momentum space depends sensitively on the geometric effects appearing in the diagnostic response function. So far, in Section 3.1, we have only considered the effect of geometry on the radiation spot shape, and not how geometric effects influence the dominant particle. The purpose of this section is therefore to characterise what is meant by "geometric effects" and explain the behaviour of the SOFT diagnostic response function, and we will do so by analysing a specific synchrotron radiation response function. As we will see, geometry generally has little effect on the radiation observed from particles with small pitch angles, but becomes increasingly important at larger particle pitch angles.

Before presenting the example response function, however, we should revisit the mathematics of the response function. The diagnostic response function was defined in Eq. (2.7), and is given in terms of an integral over the plasma volume, the detector surface and the particle gyration angle ζ. For the purpose of studying geometric effects on directed radiation, we utilise the cone approximation described in Section 2.3, and stated mathematically in Eq. (2.8). We will only be concerned with the momentum space dependence of the response function in this section, which means that we will assume that all runaway electrons are uniformly distributed in the radial coordinate ρ. Therefore, we introduce the spatially integrated response function

$$
\mathcal{G}(p_\parallel^{(0)}, p_\perp^{(0)}) = \int G(\rho, p_\parallel^{(0)}, p_\perp^{(0)})\, \mathrm{d}\rho =
$$
$$
= \iiint \Theta\left(\frac{\boldsymbol{r}}{r}\right) \frac{\boldsymbol{r} \cdot \hat{\boldsymbol{n}}}{r^3} \frac{P(\boldsymbol{x}, \boldsymbol{p})}{2\pi} \delta\left(\frac{\boldsymbol{p} \cdot \boldsymbol{r}}{pr} - 1\right)\, \mathrm{d}\zeta\, \mathrm{d}A\, \mathrm{d}V,
$$
$$(3.7)$$

where P is the total amount of emitted radiation at the point $(\boldsymbol{x}, \boldsymbol{p})$ of phase space and $\boldsymbol{p} = \boldsymbol{p}(\boldsymbol{x}, \boldsymbol{p}^{(0)})$ is the local momentum of the particle in $\boldsymbol{x}$, given initial momentum $\boldsymbol{p}^{(0)}$ at the beginning of the orbit. The coupling between the response function $\mathcal{G}$ and the magnetic field and detector geometry is evident from Eq. (3.7): only radiation inside the detector field-of-view contributes, defined through $\Theta(\boldsymbol{r}/r)$; radiation emitted further away from the detector contributes less by a factor $1/r^2$; the amount of emitted radiation $P(\boldsymbol{x}, \boldsymbol{p})$ varies in different parts of the plasma; and only radiation emitted from points on the surface-of-visibility—which results when integrating the delta function over the plasma volume—can be observed.

Although the emitted radiation P generally depends on the geometry of the setup, it is often possible to neglect this dependence and define a geometric function

$$
K(p_\parallel, p_\perp) = \frac{1}{P(\bar{\boldsymbol{x}}, p_\parallel^{(0)}, p_\perp^{(0)})} \mathcal{G}(p_\parallel^{(0)}, p_\perp^{(0)}),
\qquad (3.8)
$$

where $P(\bar{\boldsymbol{x}}, p_\parallel^{(0)}, p_\perp^{(0)})$ is the total amount of radiation *emitted* from some representative position $\bar{\boldsymbol{x}}$ in the plasma. The function K characterises the geometric effects on the detected radiation of the diagnostic setup and has the property that it reproduces $\mathcal{G}$ when multiplied with the total *emitted* radiation P. This may seem like a trivial point, but it is

in fact of great importance for constructing reduced models of the detected radiation. For example, many previous studies of the synchrotron spectrum can be seen as approximating Eq. (3.8) either as a constant or with simple functional forms [45, 80]. For our analysis, we assume $K \equiv K_0 = \text{const}$ for one of the response functions, which helps illuminate the geometric effects in the full response function $\mathcal{G}$ of Eq. (3.7).

Simulated response functions

In Table 3.3, the parameters used to simulate the two response functions are shown, and in Fig. 3.10, the corresponding response functions are plotted against the initial particle pitch angle (the superscript "(0)" has been suppressed for brevity on θ_p; all occurrences of θ_p are henceforth understood to refer to the initial pitch angle of the particle). The two response functions shown can be expressed mathematically as

$$\mathcal{G}_1(\theta_\mathrm{p}) = [\text{Equation (3.7)}]\,, \tag{3.9a}$$

$$\mathcal{G}_2(\theta_\mathrm{p}) = P(\bar{\boldsymbol{x}}, p_\parallel^{(0)}, p_\perp^{(0)})K_0. \tag{3.9b}$$

The first function, $\mathcal{G}_1$, is computed using SOFT and contains all geometric effects captured by that model. The second function, $\mathcal{G}_2$, approximates the geometric function K in Eq. (3.8) as independent of the pitch angle θ_p. We choose the point $\bar{\boldsymbol{x}}$ such that the magnetic field strength there is the maximum experienced by any particle along its orbit. This should be a good approximation for synchrotron radiation, since it depends strongly on the magnetic field strength.

We will not be concerned with the energy dependence of the response function here, as geometric effects almost exclusively appear as a pitch angle dependence. Instead, we consider both response functions at a fixed value of particle momentum p_0, chosen at the representative value $p_0 = 40 m_e c$. It should also be noted that while the following analysis is done for a specific synchrotron radiation response function, the qualitative insights gained apply also to bremsstrahlung, and a wide range of detector and magnetic field configurations.

Figure 3.10 reveals that the shape of the two response functions match relatively well at small pitch angles. At larger pitch angles, however, the growth of the SOFT response function $\mathcal{G}_1$ is limited, while $\mathcal{G}_2$ continues to grow monotonically with pitch angle. Eventually, $\mathcal{G}_1$ even

---

*The detector viewing direction is tangential to the toroidal plasma, as illustrated in Fig. 3.1.

Table 3.3: Parameters of the setup used to generate the response functions of Fig. 3.10, with and without geometric effects (GE). The parameters are chosen to make the response functions as comparable as possible, but naturally the response function taking geometric effects into account depends on more parameters.

Parameter	w/ GE	w/o GE
Magnetic field strength (on-axis) (T)	2	2.83
Particle momentum p_0 ($m_e c$)	40	40
Spectral range (µm)	3-5	3-5
Major/minor radius (m)	1.7/0.5	—
Detector aperture (m)	$6 \cdot 10^{-3}$	—
Field-of-view opening angle (rad)	0.55	—
Detector viewing direction	Tangential*	—
Detector vertical position	Midplane	—
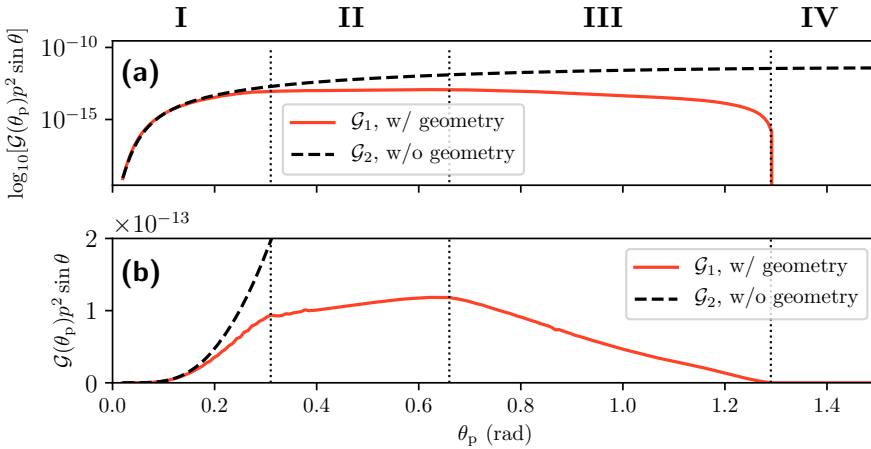
Figure 3.10: (a) Comparison of response functions simulated with and without geometric effects. Geometric effects appear to be relatively unimportant for the shape of the response function at small pitch angles, but begin to make a significant difference around $\theta_p \sim 0.30$ rad. Once they become important, they limit the detected radiation and soon cause the response function to decrease rather than increase, as is the case when geometric effects are neglected. (b) The same response functions as in (a), but plotted on a linear scale to more clearly reveal the influence of the geometric effects. For $\mathcal{G}_2$, $K_0 = 10^{-4}$.

starts to decrease and completely vanishes above some threshold pitch angle which depends on the field-of-view.

The rather complicated behaviour of the SOFT response function can be understood qualitatively by considering how the SoV is affected as the pitch angle is varied. In Fig. 3.10 we identify four regions showing very different pitch-angle dependences:

I. $\theta_\mathrm{p} \lesssim 0.30\,\mathrm{rad}$: Weak effect of geometry.

II. $\theta_\mathrm{p} \lesssim 0.65\,\mathrm{rad}$: Slowed growth of detected radiation.

III. $\theta_\mathrm{p} \lesssim 1.30\,\mathrm{rad}$: Detected radiation decreasing.

IV. $1.30\,\mathrm{rad} \lesssim \theta_\mathrm{p}$: No radiation detected.

The first region, where pitch angles are small, is the region where geometric effects are mostly negligible and the response function can be approximated according to Eq. (3.9b). Here, the full SoV is within the field-of-view of the detector. The growth of both response functions is $\sim \theta_\mathrm{p}^2$, since this is the rate at which the emitted synchrotron radiation P increases with θ_p in the considered wavelength range.

In region II, geometric effects begin to appear and limit the growth of $\mathcal{G}_1$. The reason for this can be seen also in Eq. (3.8), which at small pitch angles is

$$K(\theta_\mathrm{p}) \propto V_\mathrm{SoV} \frac{L}{L_\mathrm{C}}, \tag{3.10}$$

where V_SoV denotes the volume taken up by the SoV[†] within the plasma. The length L is the length of the circle segment of the guiding-center cone that overlaps the detector, as illustrated in Fig. 3.11, and L_C is the circumference of the whole circle. It can be shown that $V_\mathrm{SoV} \propto \theta_\mathrm{p}$ and $L/L_\mathrm{C} \propto \theta_\mathrm{p}^{-1}$, meaning that at small pitch angles $K(\theta_\mathrm{p})$ is in fact approximately constant.

At some point, the SoV will have grown so large that it extends outside the plasma. While the SoV will continue to grow with θ_p, the volume V_SoV in Eq. (3.10)—the volume of SoV that is within the plasma—will not. Rather, it shrinks as the pitch angle further increases. The transition between these two regimes is instant, and this is reflected by the discontinuity in $\mathcal{G}_1$ between region I and region II in Fig. 3.10. Exactly

---

[†]Note that the SoV, despite being referred to as a surface, occupies a volume in space when the detector has a finite surface area. The SoV is only truly a surface for a point detector.
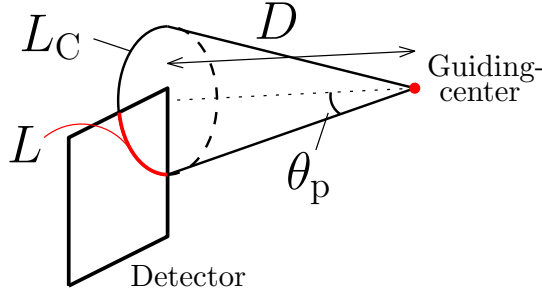
Figure 3.11: Sketch of circular segment of length L of the guiding-center cone that overlaps with the detector. The length of a cone cross-section when projected on the detector plane is denoted by L_C.

when this effect starts to impact the response function depends on the shape of the magnetic field, as well as where the detector is located relative to the plasma.

As the pitch angle further increases and we enter region III in Fig. 3.10, the SOFT response function suddenly starts to decrease. The reason for this decrease is that the SoV—which at these large pitch angles consists of two oval surfaces that move away from each other (c.f. Figs. 3.4(h) and 3.5)—has started to move out of the detector's field-of-view, and so the step function $\Theta(\boldsymbol{r}/r)$ in Eq. (3.7) starts to affect the geometric function K. The onset of this effect is mainly determined by the size of the field-of-view of the detector, but can also be affected by the shape of the tokamak wall.

Eventually, no part of the SoV is in the detector's field-of-view anymore, at which point we enter region IV in Fig. 3.10. In region IV, the detector sees no radiation, meaning that it is completely insensitive to particles with such large pitch angles. This effect can particularly impact spectrometers which often have relatively narrow fields-of-view.

As mentioned, the exact distribution of the four regions in Fig. 3.10 depends sensitively on the detector placement and magnetic field shape. The slopes of the response function also depend on the spectral range of the detector, and so the properties of a particular detector setup are difficult to predict and require simulation. Although the shapes of $\mathcal{G}_1$ and $\mathcal{G}_2$ agree relatively well at small pitch angles in the analysed scenario, agreement is not exact and could become important in certain scenarios.

Chapter 4

Summary

One of the most important concepts the plasma physicist has for studying the dynamics of runaway electrons is the electron distribution function. Unfortunately, the distribution function cannot be accessed directly in experiments; instead the runaways must be studied through measurements of associated quantities, such as the amount of current in the device or the number of emitted X-rays. On top of this, most diagnostic signals are relatively insensitive to features in the runaway electron distribution function, making detailed study of the runaways challenging.

Among the runaway electron diagnostics, bremsstrahlung and synchrotron radiation stand out by being highly sensitive to all parameters of the runaway electron distribution function. To utilise them in model validation, corresponding synthetic diagnostics must be available, and the development and subsequent application of such a numerical tool has been the focus of the research presented in this thesis. In this chapter we summarise the findings of the appended papers and comment on possible future developments.

4.1   Summary of papers

A specialisation of the model derived in Chapter 2 was presented in Paper A, along with the numerical code SOFT which implements the specialised model. The model utilises a guiding-center transformation to a reduced phase space in order to make the evaluation of the synthetic radiation diagnostic integral Eq. (2.5) more computationally feasible. Subsequent papers in this thesis can then be categorised as either

applications or extensions of that model. Papers B and D belong to the first category: Paper B used SOFT to simulate synchrotron spectra in Alcator C-Mod, while Paper D used SOFT response functions to infer the radial distribution of runaway electrons in Alcator C-Mod. Paper C belongs to both categories, as it added the ability to simulate runaway electron bremsstrahlung, while also using SOFT to analyse both the bremsstrahlung and synchrotron radiation measured during a discharge in the DIII-D tokamak.

The first application of SOFT to an experimental scenario was however already done in Paper A, where the then newly developed tool was combined with the kinetic solver CODE to study a synchrotron image taken during an Alcator C-Mod discharge. It was found that even though CODE assumes a spatially homogeneous plasma, and thus only provides the momentum-space distribution of electrons, the combined simulation was able to reproduce several features of the experimentally measured image if a radial distribution of electrons peaking on the magnetic axis and decreasing linearly with minor radius, was assumed. This comparison of simulation and experiment provides an important example of how powerful synchrotron radiation can be as a diagnostic when validating kinetic models of runaway dynamics against experiment.

Paper D extended the analysis of the Alcator C-Mod discharge done in Paper A and compared CODE and SOFT simulations with a time series of synchrotron images. Since CODE does not capture the spatial dynamics of runaways, simulations of the runaway momentum-space distribution function were supplemented with direct inversions of the radial distribution of electrons. This was facilitated through the computation of SOFT response functions which allowed Eq. (2.7) to be formulated as a linear system of equations for every pixel of the image and solved using standard methods. The inversion, combined with magnetic measurements, indicate that runaway electrons may be trapped in a 2/1 magnetic island and expelled due to increased radial transport during the discharge. The use of synchrotron radiation is therefore not necessarily limited to validating kinetic models of runaway electrons, but could also be used to directly infer parts of the runaway electron dynamics.

SOFT was also used to study the impact of magnetic field strength on the runaway dynamics in Paper B. There, a set of Alcator C-Mod discharges were analysed by looking, in particular, at measured synchrotron spectra. Using SOFT, it was possible to test the predictions for the runaway dynamics made by a test-particle model [88] and CODE against

experimentally measured synchrotron spectra, and use these models to determine how the runaway energy scales with magnetic field strength. In addition to Soft, the synchrotron emission code Syrup [80] was also used to compute spectra. While it was shown that Soft was needed to reproduce the synchrotron spectra at higher magnetic field strengths, it was only possible to explain the spectrum evolution at the highest field strength at later times. One possible explanation for the lack of agreement at higher fields that was put forward was that runaway electron drift orbits became significant enough to alter the spectrum—the spectrometer's field-of-view is small enough that a radial shift of the electrons could change the dominant runaway parameters of the spectrum.

In Paper C, the most important features of directed radiation images were reviewed, and demonstrated on bremsstrahlung and synchrotron images taken in the DIII-D tokamak. The surface-of-visibility concept was discussed, and it was shown how the strong magnetic field dependence of synchrotron radiation can lead to distorted spot shapes, with most radiation seen on the high-field side of the tokamak. Altogether, this explains the crescent synchrotron spot shape often observed in many tokamaks, including in DIII-D.

A kinetic simulation of a DIII-D discharge was also conducted using Code, and validated against experiment. Despite assuming different forms for the radial distribution of electrons, little agreement was found between simulation and experiment. However, taking all particles to have the same energy, but being distributed in pitch-angle, provided better agreement with experiment. Hence, together with evidence from Refs. [47, 48], it was suggested that kinetic processes not included in Code may be contributing to the runaway dynamics in this scenario. Possible such processes include radial transport and kinetic instabilities.

Paper C also described the implementation of bremsstrahlung into Soft, which was demonstrated for the Gamma Ray Imager (GRI) diagnostic, installed at DIII-D, which is able to produce bremsstrahlung camera images. It was shown that due to the completely different energy and pitch-angle dependence of bremsstrahlung, along with the lack of magnetic field dependence, the same runaway electron distribution function can give rise to completely different bremsstrahlung and synchrotron radiation spot shapes. This, however, also means that the two types of radiation probe different parts of the distribution function, and can therefore act as complementary diagnostics to study a larger part of momentum space.

4.2 Outlook

With numerical tools such as SOFT available for simulating bremsstrahlung and synchrotron radiation from runaway electrons, quantitative comparisons of experimental measurements against distribution functions from state-of-the-art kinetic models can now be carried out. As evidenced by the work in this thesis, these comparisons have already proven useful in interpreting several experimental observations, but have also hinted at limitations of the current version of SOFT. One important effect that is currently not treated in the model is the drift motion experienced by the guiding-center. At the high particle energies that runaways typically possess, these orbit drifts can sometimes significantly alter the orbit shape, and are therefore expected to alter the shape of the observed radiation spot accordingly. To rigorously account for drift orbits however, the current theory must be extended to the next order in guiding-center theory, as drifts are formally a first order effect.

The extension to higher order is not straightforward, as the emitted radiation explicitly depends on the position and momentum vectors of the *particle*, and not just the guiding-center position and momentum. This means that the emitted radiation will depend on the shape of the gyration orbit of the particle around the guiding-center, which in the lowest order theory just traces a circle in the plane perpendicular to the magnetic field. To higher order, the gyro orbit receives corrections that break the gyro orbit isotropy. As a consequence, the computationally very efficient cone model may not be applicable in certain scenarios where drifts become important, because the cone approximation relies precisely on the fact that the gyro orbit is circular in lowest order. A non-circular gyro-orbit leads to a non-circular cone of emission, which affects at which points of space the runaways are observed by a detector. An estimate of the importance of this effect was made in Paper H which suggested that in certain scenarios it may actually be significant enough to enhance or completely cancel the radial shift of particles due to guiding-center drifts. On the other hand, in a recent study [89] of the guiding-center motion of runaway electrons, it was shown that the gyro orbits of runaway electrons are in fact circular even to second order, if the runaway electron pitch angle is also assumed small. A full study of the importance of the effect, and to what extent the assumptions of the cone approximation are valid, remains to be conducted.

An alternative approach to validating the cone model when drift orbits are included is to compare SOFT simulations to corresponding

full-orbit simulations, with e.g. KORC [70, 81] or a similar model. This would also help to validate the SOFT model as a whole and help estimate its accuracy in various scenarios. Recently, concerns about the non-conservation of the first-order guiding-center magnetic moment in runaway electrons have been raised [81, 90], suggesting that the regular guiding-center equations of motion may not be valid for those particles. Since this is what is used in SOFT to parameterise phase space, a full-orbit benchmark could help to discern in which scenarios a tool such as SOFT would not be applicable.

Most of the work in this thesis has focused on so-called forward modelling of the runaway electron radiation—i.e. producing diagnostic signals from a given distribution function. In Paper D, however, the opposite problem was considered and the radial distribution of runaway electrons was directly inferred from synchrotron images. In the past, several studies attempted inversions of the runaway electron energy distribution from bremsstrahlung measurements [47, 71, 73, 74]. While these studies were limited to one phase space parameter, it should be possible to extend them to more parameters. The inverse problem for observed radiation is however ill-posed, and standard matrix inversions are usually not possible [72]. Instead, more sophisticated methods must be applied that allow physical constraints to be set, and that utilise all available measurements. Since bremsstrahlung and synchrotron radiation probe different parts of momentum space, utilising both signals for inversions should put the needed constraints on the possible shape of the distribution function. Similar techniques have been applied to invert the fast-ion distribution function in fusion plasmas previously [91–94], and could serve as inspiration for an application to runaway electrons.

Already, runaway electron bremsstrahlung and synchrotron radiation modelling has come a long way, and the suggestions discussed above would further strengthen the utility of bremsstrahlung and synchrotron for diagnosing runaway electrons. With the first plasma in ITER approaching, the urgency of the runaway issue is becoming more and more apparent. The only way in which we can solve the problem is to continue to improve our knowledge about runaway electrons, which, in the end, means developing better models for their dynamics and validating them against experiments. It is clear that both bremsstrahlung and synchrotron radiation have important roles to play in the validation of such models, and to that end the work presented in this thesis provides a firm basis for future studies.

References

[1] IPCC. *Climate Change 2013: The physical science basis. Contribution of Working Group I to the Fifth Assessment Report of the Intergovernmental Panel on Climate Change.* Cambridge, United Kingdom and New York, NY, USA, 2013. DOI: `10.1017/CBO 9781107415324`.

[2] J. P. Freidberg. *Plasma physics and fusion energy.* Cambridge University Press, 2008.

[3] T. C. Hender et al. "Chapter 3: MHD stability, operational limits and disruptions". In: *Nuclear Fusion* 47.6 (2007), S128. DOI: `10.1088/0029-5515/47/6/S03`.

[4] F. C. Schüller. "Disruptions in tokamaks". In: *Plasma Physics and Controlled Fusion* 37.11A (1995), A135. DOI: `10.1088/0741-3335/37/11A/009`.

[5] A. H. Boozer. "Theory of tokamak disruptions". In: *Physics of plasmas* 19.5 (2012), p. 058101. DOI: `10.1063/1.3703327`.

[6] P. Helander and D. J. Sigmar. *Collisional transport in magnetized plasmas.* Cambridge, UK: Cambridge University Press, 2002.

[7] J. D. Jackson. *Classical electrodynamics.* 3rd ed. John Wiley & Sons, 2012.

[8] T. G. Northrop. "The guiding center approximation to charged particle motion". In: *Annals of Physics* 15.1 (1961), p. 79. DOI: `10.1016/0003-4916(61)90167-1`.

[9] T. Fülöp, G. Pokol, P. Helander, and M. Lisak. "Destabilization of magnetosonic-whistler waves by a relativistic runaway beam". In: *Physics of Plasmas* 13.6 (2006), p. 062506. DOI: `10.1063/1.2208327`.

[10] M. Landreman, A. Stahl, and T. Fülöp. "Numerical calculation of the runaway electron distribution function and associated synchrotron emission". In: *Computer Physics Communications* 185.3 (2014), p. 847. DOI: `10.1016/j.cpc.2013.12.004`.

[11] A. Stahl, O. Embréus, G. Papp, M. Landreman, and T. Fülöp. "Kinetic modelling of runaway electrons in dynamic scenarios". In: *Nuclear Fusion* 56.11 (2016), p. 112009. DOI: `10.1088/0029-5515/56/11/112009`.

[12] C. T. R. Wilson. "The electric field of a thundercloud and some of its effects". In: *Proceedings of the Physical Society of London* 37.1 (1924), p. 32D. DOI: `10.1088/1478-7814/37/1/314`.

[13] H. Dreicer. "Electron and ion runaway in a fully ionized gas. I". In: *Physical Review* 115 (1959), p. 238. DOI: `10.1103/PhysRev.115.238`.

[14] H. Dreicer. "Electron and ion runaway in a fully ionized gas. II". In: *Physical Review* 117 (1960), p. 329. DOI: `10.1103/PhysRev.117.329`.

[15] J. W. Connor and R. J. Hastie. "Relativistic limitations on runaway electrons". In: *Nuclear Fusion* 15.3 (1975), p. 415. DOI: `10.1088/0029-5515/15/3/007`.

[16] A. Stahl, E. Hirvijoki, J. Decker, O. Embréus, and T. Fülöp. "Effective critical electric field for runaway-electron generation". In: *Physical Review Letters* 114 (2015), p. 115002. DOI: `10.1103/PhysRevLett.114.115002`.

[17] L. Hesslow, O. Embréus, G. J. Wilkie, G. Papp, and T. Fülöp. "Effect of partially ionized impurities and radiation on the effective critical electric field for runaway generation". In: *Plasma Physics and Controlled Fusion* 60.7 (2018), p. 074010. DOI: `https://doi.org/10.1103/PhysRevLett.118.255001`.

[18] J. R. Martín-Solís, R. Sánchez, and B. Esposito. "Experimental observation of increased threshold electric field for runaway generation due to synchrotron radiation losses in the FTU tokamak". In: *Physical Review Letters* 105 (2010), p. 185002. DOI: `10.1103/PhysRevLett.105.185002`.

[19] R. S. Granetz et al. "An ITPA joint experiment to study runaway electron generation and suppression". In: *Physics of Plasmas* 21.7 (2014), p. 072506. DOI: `10.1063/1.4886802`.

[20]   C. Paz-Soldan et al. "Growth and decay of runaway electrons above the critical electric field under quiescent conditions". In: *Physics of Plasmas* 21.2 (2014), p. 022514. DOI: 10.1063/1.4866912.

[21]   G. D. Holman. "Acceleration of runaway electrons and Joule heating in solar flares". In: *The Astrophysical Journal* 293 (1985), p. 584. DOI: 10.1086/163263.

[22]   N. G. Lehtinen, T. F. Bell, and U. S. Inan. "Monte Carlo simulation of runaway MeV electron breakdown with application to red sprites and terrestrial gamma ray flashes". In: *Journal of Geophysical Research: Space Physics* 104.A11 (1999), p. 24699. DOI: 10.1029/1999JA900335.

[23]   J. R. Dwyer. "Relativistic breakdown in planetary atmospheres". In: *Physics of Plasmas* 14.4 (2007), p. 042901. DOI: 10.1063/1.2709652.

[24]   P. Helander, L.-G. Eriksson, and F. Andersson. "Runaway acceleration during magnetic reconnection in tokamaks". In: *Plasma Physics and Controlled Fusion* 44.12B (2002), B247. DOI: 10.1088/0741-3335/44/12B/318.

[25]   J. Wesson and D. J. Campbell. *Tokamaks*. Vol. 149. Oxford University Press, 2011.

[26]   J. A. Wesson et al. "Disruptions in JET". In: *Nuclear Fusion* 29.4 (1989), p. 641. DOI: 10.1088/0029-5515/29/4/009.

[27]   P. C. De Vries et al. "Survey of disruption causes at JET". In: *Nuclear Fusion* 51.5 (2011), p. 053018. DOI: 10.1088/0029-5515/51/5/053018.

[28]   S. C. Chiu, M. N. Rosenbluth, R. W. Harvey, and V. S. Chan. "Fokker-Planck simulations mylb of knock-on electron runaway avalanche and bursts in tokamaks". In: *Nuclear Fusion* 38.11 (1998), p. 1711. DOI: 10.1088/0029-5515/38/11/309.

[29]   P. Helander, H. Smith, T. Fülöp, and L.-G. Eriksson. "Electron kinetics in a cooling plasma". In: *Physics of Plasmas* 11.12 (2004), pp. 5704–5709. DOI: 10.1063/1.1812759.

[30]   H. Smith, P. Helander, L.-G. Eriksson, and T. Fülöp. "Runaway electron generation in a cooling plasma". In: *Physics of Plasmas* 12.12 (2005), p. 122505. DOI: 10.1063/1.2148966.

[31] H. M. Smith and E. Verwichte. "Hot tail runaway electron genera-
      tion in tokamak disruptions". In: *Physics of Plasmas* 15.7 (2008),
      p. 072502. DOI: 10.1063/1.2949692.

[32] P. Aleynikov and B. N. Breizman. "Generation of runaway elec-
      trons during the thermal quench in tokamaks". In: *Nuclear Fusion*
      57.4 (2017), p. 046009. DOI: 10.1088/1741-4326/aa5895.

[33] I. U. A. Sokolov. ""Multiplication" of accelerated electrons in a
      tokamak". In: *JETP Letters* 29 (1979), p. 218.

[34] R. Jayakumar, H. H. Fleischmann, and S. J. Zweben. "Collisional
      avalanche exponentiation of runaway electrons in electrified plas-
      mas". In: *Physics Letters A* 172.6 (1993), pp. 447–451. DOI: 10.
      1016/0375-9601(93)90237-T.

[35] M. N. Rosenbluth and S. V. Putvinski. "Theory for avalanche of
      runaway electrons in tokamaks". In: *Nuclear Fusion* 37.10 (1997),
      p. 1355. DOI: 10.1088/0029-5515/37/10/I03.

[36] O. Embréus, A. Stahl, and T. Fülöp. "On the relativistic large-
      angle electron collision operator for runaway avalanches in plas-
      mas". In: *Journal of Plasma Physics* 84.1 (2018), p. 905840102.
      DOI: 10.1017/S002237781700099X.

[37] M. Lehnen et al. "Disruptions in ITER and strategies for their con-
      trol and mitigation". In: *Journal of Nuclear Materials* 463 (2015),
      p. 39. DOI: 10.1016/j.jnucmat.2014.10.075.

[38] F. Andersson, P. Helander, and L.-G. Eriksson. "Damping of rel-
      ativistic electron beams by synchrotron radiation". In: *Physics of
      Plasmas* 8.12 (2001), p. 5221. DOI: 10.1063/1.1418242.

[39] E. Hirvijoki, I. Pusztai, J. Decker, O. Embréus, A. Stahl, and T.
      Fülöp. "Radiation reaction induced non-monotonic features in run-
      away electron distributions". In: *Journal of Plasma Physics* 81.5
      (2015), p. 475810502. DOI: 10.1017/S0022377815000513.

[40] J. Decker et al. "Numerical characterization of bump formation
      in the runaway electron tail". In: *Plasma Physics and Controlled
      Fusion* 58.2 (2016), p. 025016. DOI: 10.1088/0741-3335/58/2/
      025016.

[41] O. Embréus, A. Stahl, and T. Fülöp. "Effect of bremsstrahlung
      radiation emission on fast electrons in plasmas". In: *New Journal
      of Physics* 18.9 (2016), p. 093023. DOI: 10.1088/1367-2630/18/
      9/093023.

[42] K. H. Finken et al. "Observation of infrared synchrotron radiation from tokamak runaway electrons in TEXTOR". In: *Nuclear Fusion* 30.5 (1990), p. 859. DOI: 10.1088/0029-5515/30/5/005.

[43] G. Papp et al. "Runaway electron generation and mitigation on the European medium sized tokamaks ASDEX Upgrade and TCV". In: *Proceedings of the 2016 IAEA Fusion Energy Conference*. EX/9-4. Kyoto, Japan, 2016.

[44] M. Vlainic et al. "Post-disruptive runaway electron beams in the COMPASS tokamak". In: *Journal of Plasma Physics* 81.5 (2015), p. 475810506. DOI: 10.1017/S0022377815000914.

[45] J. H. Yu et al. "Visible imaging and spectroscopy of disruption runaway electrons in DIII-D". In: *Physics of Plasmas* 20.4 (2013), p. 042113. DOI: 10.1063/1.4801738.

[46] E. M. Hollmann et al. "Measurement of runaway electron energy distribution function during high-Z gas injection into runaway electron plateaus in DIII-D". In: *Physics of Plasmas* 22.5 (2015), p. 056108. DOI: 10.1063/1.4921149.

[47] C. Paz-Soldan et al. "Spatiotemporal evolution of runaway electron momentum distributions in tokamaks". In: *Physical Review Letters* 118 (2017), p. 255002. DOI: 10.1103/PhysRevLett.118.255002.

[48] C. Paz-Soldan et al. "Resolving runaway electron distributions in space, time, and energy". In: *Physics of Plasmas* 25.5 (2018), p. 056105. DOI: 10.1063/1.5024223.

[49] Y. Shi et al. "Observation of runaway electron beams by visible color camera in the Experimental Advanced Superconducting Tokamak". In: *Review of Scientific Instruments* 81.3 (2010), p. 033506. DOI: 10.1063/1.3340909.

[50] R. J. Zhou et al. "Investigation of ring-like runaway electron beams in the EAST tokamak". In: *Plasma Physics and Controlled Fusion* 55.5 (2013), p. 055006. DOI: 10.1088/0741-3335/55/5/055006.

[51] R. J. Zhou, I. M. Pankratov, L. Q. Hu, M. Xu, and J. H. Yang. "Synchrotron radiation spectra and synchrotron radiation spot shape of runaway electrons in Experimental Advanced Superconducting Tokamak". In: *Physics of Plasmas* 21.6 (2014), p. 063302. DOI: 10.1063/1.4881469.

[52]   B. Esposito et al. "Runaway electron generation and control". In: *Plasma Physics and Controlled Fusion* 59.1 (2017), p. 014044. DOI: `10.1088/0741-3335/59/1/014044`.

[53]   Y. P. Zhang et al. "Observation of the generation and evolution of long-lived runaway electron beams during major disruptions in the HuanLiuqi-2A tokamak". In: *Physics of Plasmas* 19.3 (2012), p. 032510. DOI: `10.1063/1.3696073`.

[54]   Z. Y. Chen et al. "Measurement of the runaway electrons in the HT-7 tokamak". In: *Review of Scientific Instruments* 77.1 (2006), p. 013502. DOI: `10.1063/1.2140488`.

[55]   R. H. Tong, Z. Y. Chen, M. Zhang, D. W. Huang, W. Yan, and G. Zhuang. "Observation of runaway electrons by infrared camera in J-TEXT". In: *Review of Scientific Instruments* 87.11 (2016), 11E113. DOI: `10.1063/1.4960311`.

[56]   A. C. England et al. "Runaway electron suppression by ECRH and RMP in KSTAR". In: *Plasma Science and Technology* 15.2 (2013), p. 119. DOI: `10.1088/1009-0630/15/2/08`.

[57]   R. Jaspers et al. "Experimental investigation of runaway electron generation in TEXTOR". In: *Nuclear Fusion* 33.12 (1993), p. 1775. DOI: `10.1088/0029-5515/33/12/I02`.

[58]   R. Jaspers et al. "Islands of runaway electrons in the TEXTOR tokamak and relation to transport in a stochastic field". In: *Physical Review Letters* 72 (1994), p. 4093. DOI: `10.1103/PhysRevLett.72.4093`.

[59]   I. Entrop, N. J. Lopes Cardozo, R. Jaspers, and K. H. Finken. "Diffusion of runaway electrons in TEXTOR-94". In: *Plasma Physics and Controlled Fusion* 40.8 (1998), p. 1513. DOI: `10.1088/0741-3335/40/8/005`.

[60]   I. Entrop, R. Jaspers, N. J. Lopes Cardozo, and K. H. Finken. "Runaway snakes in TEXTOR-94". In: *Plasma Physics and Controlled Fusion* 41.3 (1999), p. 377. DOI: `10.1088/0741-3335/41/3/004`.

[61]   S A Bozhenkov et al. "Generation and suppression of runaway electrons in disruption mitigation experiments in TEXTOR". In: *Plasma Physics and Controlled Fusion* 50.10 (2008), p. 105007. DOI: `10.1088/0741-3335/50/10/105007`.

[62] T. Kudyakov et al. "Influence of B_t on the magnetic turbulence and on the runaway transport in low-density discharges". In: *Nuclear Fusion* 52.2 (2012), p. 023025. DOI: `10.1088/0029-5515/52/2/023025`.

[63] K. Wongrach et al. "Measurement of synchrotron radiation from runaway electrons during the TEXTOR tokamak disruptions". In: *Nuclear Fusion* 54.4 (2014), p. 043011. DOI: `10.1088/0029-5515/54/4/043011`.

[64] K. Wongrach et al. "Runaway electron studies in TEXTOR". In: *Nuclear Fusion* 55.5 (2015), p. 053008. DOI: `10.1088/0029-5515/55/5/053008`.

[65] R. E. Jaspers. "Relativistic runaway electrons in tokamak plasmas". PhD thesis. 1995.

[66] I. M. Pankratov. "Analysis of the synchrotron radiation emitted by runaway electrons". In: *Plasma Physics Reports* 22.6 (1996), p. 535.

[67] I. M. Pankratov. "Analysis of the synchrotron radiation spectra of runaway electrons". In: *PLASMA PHYSICS REPORTS C/C OF FIZIKA PLAZMY* 25 (1999), p. 145.

[68] I. Entrop. "Confinement of relativistic runaway electrons in tokamak plasmas". PhD thesis. 1999. DOI: `10.6100/IR528445`.

[69] R. Jaspers, N. J. Lopes Cardozo, A. J. H. Donné, H. L. M. Widdershoven, and K. H. Finken. "A synchrotron radiation diagnostic to observe relativistic runaway electrons in a tokamak plasma". In: *Review of Scientific Instruments* 72.1 (2001), p. 466. DOI: `10.1063/1.1318245`.

[70] L. Carbajal and D. del-Castillo-Negrete. "On the synchrotron emission in kinetic simulations of runaway electrons in magnetic confinement fusion plasmas". In: *Plasma Physics and Controlled Fusion* 59.12 (2017), p. 124001. DOI: `10.1088/1361-6587/aa883e`.

[71] Y. Peysson and F. Imbeaux. "Tomography of the fast electron bremsstrahlung emission during lower hybrid current drive on TORE SUPRA". In: *Review of Scientific Instruments* 70.10 (1999), p. 3987. DOI: `10.1063/1.1150025`.

[72] Y. Peysson and J. Decker. "Fast electron bremsstrahlung in axisymmetric magnetic configuration". In: *Physics of Plasmas* 15.9 (2008), p. 092509. DOI: `10.1063/1.2981391`.

[73] A. E. Shevelev et al. "Reconstruction of distribution functions of fast ions and runaway electrons in fusion plasmas using gamma-ray spectrometry with applications to ITER". In: *Nuclear Fusion* 53.12 (2013), p. 123004. DOI: 10.1088/0029-5515/53/12/123004.

[74] A. E. Shevelev et al. "Runaway electron studies with hard x-ray and microwave diagnostics in the FT-2 lower hybrid current drive discharges". In: *Nuclear Fusion* 58.1 (2018), p. 016034. DOI: 10.1088/1741-4326/aa8cea.

[75] D. C. Pace et al. "Gamma ray imager on the DIII-D tokamak". In: *Review of Scientific Instruments* 87.4 (2016), p. 043507. DOI: 10.1063/1.4945566.

[76] C. M. Cooper et al. "Applying the new gamma ray imager diagnostic to measurements of runaway electron Bremsstrahlung radiation in the DIII-D Tokamak (invited)". In: *Review of Scientific Instruments* 87.11 (2016), 11E602. DOI: 10.1063/1.4961288.

[77] W. Rindler. *Relativity: special, general, and cosmological.* 2nd ed. Oxford, UK: Oxford University Press, 2006.

[78] F. R. Elder, A. M. Gurewitsch, R. V. Langmuir, and H. C. Pollock. "Radiation from electrons in a synchrotron". In: *Physical Review* 71.11 (1947), p. 829. DOI: 10.1103/PhysRev.71.829.5.

[79] J. Schwinger. "On the classical radiation of accelerated electrons". In: *Physical Review* 75.12 (1949), p. 1912. DOI: 10.1103/PhysRev.75.1912.

[80] A. Stahl, M. Landreman, G. Papp, E. Hollmann, and T. Fülöp. "Synchrotron radiation from a runaway electron distribution in tokamaks". In: *Physics of Plasmas* 20.9 (2013), p. 093302. DOI: 10.1063/1.4821823.

[81] L. Carbajal, D. del-Castillo-Negrete, D. Spong, S. Seal, and L. Baylor. "Space dependent, full orbit effects on runaway electron dynamics in tokamak plasmas". In: *Physics of Plasmas* 24.4 (2017), p. 042512. DOI: 10.1063/1.4981209.

[82] R. G. Littlejohn. "Hamiltonian formulation of guiding center motion". In: *The Physics of Fluids* 24.9 (1981), p. 1730. DOI: 10.1063/1.863594.

[83] X. Tao, A. A. Chan, and A. J. Brizard. "Hamiltonian theory of adiabatic motion of relativistic charged particles". In: *Physics of Plasmas* 14.9 (2007), p. 092107. DOI: 10.1063/1.2773702.

[84]   R. W. Harvey, V. S. Chan, S. C. Chiu, T. E. Evans, M. N. Rosen-bluth, and D. G. Whyte. "Runaway electron production in DIII-D killer pellet experiments, calculated with the CQL3D/KPRAD model". In: *Physics of Plasmas* 7.11 (2000), p. 4590. DOI: 10.1063/1.1312816.

[85]   Y. V. Petrov and R. W. Harvey. "A fully-neoclassical finite-orbit-width version of the CQL3D Fokker–Planck code". In: *Plasma Physics and Controlled Fusion* 58.11 (2016), p. 115001. DOI: 10.1088/0741-3335/58/11/115001.

[86]   Y. Peysson, J. Decker, and R. W. Harvey. "Advanced 3-D electron Fokker-Planck transport calculations". In: *AIP Conference Proceedings* 694.1 (2003), p. 495. DOI: 10.1063/1.1638086.

[87]   J. Decker and Y. Peysson. *DKE: a fast numerical solver for the 3D drift kinetic equation.* Tech. rep. No EUR-CEA-FC-1736, 2004.

[88]   J. R. Martín-Solís, J. D. Alvarez, R. Sánchez, and B. Esposito. "Momentum–space structure of relativistic runaway electrons". In: *Physics of Plasmas* 5.6 (1998), pp. 2370–2377. DOI: 10.1063/1.872911.

[89]   C. Liu, H. Qin, E. Hirvijoki, Y. Wang, and J. Liu. "Conservative magnetic moment of runaway electrons and collisionless pitch-angle scattering". In: *Nuclear Fusion* 58.10 (2018), p. 106018. DOI: 10.1088/1741-4326/aad2a5.

[90]   J. Liu, Y. Wang, and H. Qin. "Collisionless pitch-angle scattering of runaway electrons". In: *Nuclear Fusion* 56.6 (2016), p. 064002. DOI: 10.1088/0029-5515/56/6/064002.

[91]   M. Salewski et al. "Tomography of fast-ion velocity-space distributions from synthetic CTS and FIDA measurements". In: *Nuclear Fusion* 52.10 (2012), p. 103008. DOI: 10.1088/0029-5515/52/10/103008.

[92]   M. Salewski et al. "Measurement of a 2D fast-ion velocity distribution function by tomographic inversion of fast-ion D-alpha spectra". In: *Nuclear Fusion* 54.2 (2014), p. 023005. DOI: 10.1088/0029-5515/54/2/023005.

[93]   A. S. Jacobsen et al. "Inversion methods for fast-ion velocity-space tomography in fusion plasmas". In: *Plasma Physics and Controlled Fusion* 58.4 (2016), p. 045016. DOI: 10.1088/0741-3335/58/4/045016.

[94]   M. Salewski et al. "High-definition velocity-space tomography of fast-ion dynamics". In: *Nuclear Fusion* 56.10 (2016), p. 106024. DOI: 10.1088/0029-5515/56/10/106024.